

A Director-Field Theory of DNA Packaging in Bacteriophage Viruses

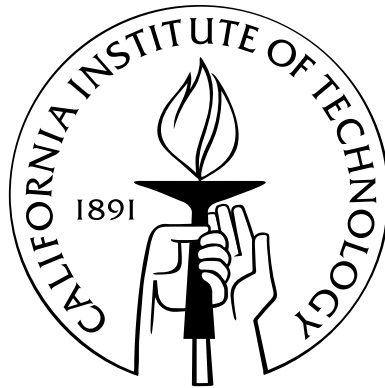
Thesis by

William Scott Klug

In Partial Fulfillment of the Requirements

for the Degree of

Doctor of Philosophy



California Institute of Technology

Pasadena, California

2003

(Defended August 27, 2003)

© 2003

William Scott Klug

All Rights Reserved

To Mary Elise.

Acknowledgements

First of all, I am grateful for the opportunity to have worked with and learned from my advisor, Michael Ortiz. He has guided me through the academic challenges which have inspired my best work, and has consistently supported all of my academic and professional endeavors. I have been strongly affected by his excitement for scientific research, and diversity of academic interests. Similarly I am indebted to my friend and former advisor from UCLA, Lew Felton. He has provided constant support and guidance, encouraging me to pursue my academic and career dreams. I am also thankful to have known and worked with Rob Phillips, who has freely shared his time, thoughts, and enthusiasm for scientific discovery.

Prashant Purohit has welcomed conversation about DNA and viruses, pointing out some especially helpful references. Mike Feldmann and Anna Pandolfi have each been especially generous, assisting in this research through thought, discussion, and even a bit of coding. Their help has been greatly appreciated.

I am thankful for the friendships I've enjoyed at Caltech. I maintained my sanity through many a round of Guinness with Jeff and Arash; Lunch-time hoops and trips to Ernie's with Andy; countless conversations about research, Linux, and computers with Alejandro over lunch at Wahoo's and El Toreo. I have enjoyed time spent with my office-mates past and present: Olga, Adrian, Matias, Matt, John, Puru, and Marisol. Lydia deserves special thanks, for her help with countless tasks, and for many friendly conversations.

I owe special thanks to my family. My parents, Jane and Ken, have taught me how to work, and how to live. They, along with my brothers, Jeff and Andrew, have always loved, encouraged, and supported me. I am also grateful for two super parents-in-law, Katy and Rick, who have shared their love, encouragement, and support as well.

Finally, my wife, Mary Elise, deserves credit for my successes every bit as much as I do. She has stood by my side through my entire graduate education, making untold sacrifices graciously and without complaint. From before the day my acceptance letter arrived from Caltech to this day, she has encouraged me and loved me unconditionally. So, pal, this is for you.

Abstract

This thesis is concerned with the formulation of a continuum theory of packaging of DNA in bacterial viruses based on a director-field representation of the encapsidated DNA. The point values of the director field give the local direction and density of the DNA. The continuity of the DNA strand requires that the director field be divergence-free and tangent to the capsid wall. The energy of the DNA is defined as a functional of the director field which accounts for bending, torsion, and for electrostatic interactions through a density-dependent interaction energy. The operative principle which determines the encapsidated DNA conformation is assumed to be energy minimization.

The director-field theory is used for the direct formulation and study of two low-energy DNA conformations: the inverse spool and torsionless toroidal solenoids. Analysis of the inverse spool configuration yields predictions of the interaxial spacing and the dependence of the packing force on the packed genome fraction which are found to be in agreement with experiments. Further analysis shows that torsionless toroidal solenoids can achieve lower energy than the inverse spool configuration.

Also, the theory is adapted to a framework of numerical optimization, wherein all fields are discretized on a computational lattice, and energy minimizing configurations are sought via simulated annealing and the nonlinear conjugate gradient method. It is shown that the inverse spool conformation is stable in all regions of the virus capsid except in a central core, where the DNA tends to *buckle* out of the spooling plane.

Contents

Acknowledgements	iv
Abstract	vi
1 Introduction	1
2 The Theory	6
2.1 Director-field description	7
2.2 Energetics of packaged DNA	9
2.2.1 Elastic energy	10
2.2.2 Interaction energy	11
2.2.3 Total energy and variational problem	18
2.3 Summary	21
3 Constructions	23
3.1 Inverse spool construction	24
3.1.1 Application to the $\phi 29$ bacteriophage	26
3.1.2 Surface energy	28
3.2 Torsionless toroidal solenoids	38
3.3 Solenoid/spool mixtures	46
3.3.1 Equilibrium solenoid/spool interfaces	47
3.3.2 Fine solenoid/spool mixtures	50
3.3.3 Application to the $\phi 29$ bacteriophage	54
3.4 Summary	57

4	Numerical Optimization	58
4.1	Discrete problem	59
4.1.1	Constraints	61
4.1.2	Minimization problem	62
4.2	Numerical methods	63
4.2.1	Simulated annealing	63
4.2.2	The nonlinear conjugate gradient method	66
4.3	Optimization in two dimensions	67
4.3.1	Bacteriophage $\phi 29$	68
4.4	Optimization in three dimensions	72
4.4.1	Simulated annealing	73
4.4.2	Conjugate gradients	74
4.5	Summary	75
5	Conclusion	78
A	Configurational forces	81
B	An iterative front-relaxation algorithm	85

List of Figures

1.1	Cryo-electron microscopy images of the T4 bacteriophage reprinted from (Olson et al., 2001), Copyright 2001, with permission from Elsevier. (a) Shaded-surface rendering of the three-dimensional reconstruction of a filled T4 virus. (b) Central section of the reconstructed T4 density map (high-density features appear dark).	3
1.2	Cryo-electron micrograph and computer-processed images of T7 bacteriophage reprinted from (Cerritelli et al., 1997), Copyright 1997, with permission from Elsevier. (a) Cryo-electron micrograph of a field of bacteriophage T7 heads. The concentric ring motif is evident in virus viewed along the axis through the portal and the center of the virus (e.g., the virus indexed with a single closed circle). Scale bar = 50 nm. (b) Two axial views at higher magnification. Scale bar = 25 nm. (c and d) Images obtained by averaging 21 and 77 viruses, respectively.	4
2.1	a) Director-field representation of the geometry of a DNA condensate. b) Director-field definition in terms of DNA flux through an oriented surface S	7
2.2	Repulsive interaction potential. $F_0 = 55000$ pN/nm ² and $c = 0.28$ nm.	12
2.3	Attractive interaction potential. $e_0 = 0.12k_B T/\text{nm}$, $\phi_0 = 0.12k_B T/\text{nm}^2$ and $c = 0.28$ nm.	14
2.4	Dual of attractive DNA interaction energy function vs. chemical potential.	17
3.1	Geometry of the inverse-spool conformation.	24

3.2	Density $u(r, F)$ for a $\phi 29$ capsid with fully repulsive potential: $F \in [0, 60pN]$ and $r \in [0, 21nm]$. a) Contour plot; dark indicates low density, light indicates high density. b) 3-D surface plot.	28
3.3	Density and spacing for $\phi 29$ with fully repulsive potential: (a) Density vs. force at the outer radius $R = 21$ nm. (b) Spacing vs. force at the outer radius $R = 21$ nm. (c) Density vs. radius at full packing. (d) Spacing vs. radius at full packing.	29
3.4	Inverse spool construction. a) Assumed geometry of $\phi 29$ bacteriophage. b) Internal force vs. fraction of genome packaged.	30
3.5	Inverse spool modeled with surface energy effects.	31
3.6	Surface contours of DNA at different forces within the $\phi 29$ capsid. (Axes measure position in nm.)	37
3.7	Geometry of torsionless toroidal solenoid.	39
3.8	Schematic of characteristic construction for the solenoid DNA conformation.	41
3.9	Torsionless toroidal solenoid of circular cross section.	45
3.10	Equilibrium spool/solenoid interface.	49
3.11	a) Relaxation of concave segments of an initial front to equilibrium interface segments. b) Closeup of the initial and relaxed fronts and the resulting spool gap.	53
3.12	a) DNA conformation within a $\phi 29$ bacteriophage predicted by the mixed solenoid/spool construction. The conformation contains a solenoid/spool mixture region near the apices; spool pockets near the apices and shoulder of the capsid; and a spool core. b) Closeup of the apex of the capsid. c) Closeup of the solenoid/spool mixture at the apex of the capsid, consisting of a complex arrangement of alternating solenoid bundles and spool gaps. d) Closeup of the shoulder of the capsid, showing the relaxation of the initial front toward an equilibrium interface, the intervening spool gap, the subsequent solenoid bundle, and the spool core.	55
4.1	Diagram of an embedded computational grid model of a $\phi 29$ bacteriophage.	59

4.2	Log-log plot of the height-normalized minimum energy, E_{\min}/h vs. the number of trial states generated by the annealing algorithm.	69
4.3	Several of the configurations produced in the annealing “temperature trials.” .	70
4.4	Lowest-energy 2-D conformation. (a) Conformation attained with FSA. (b) Annealed conformation after further optimization with CG.	72
4.5	Lattice models of a bacteriophage λ : (a) 10 points per edge, (b) 20 points per edge	73
4.6	Results of FSA applied to spool configuration on 10-point-per-edge lattice: (a) Full view, (b) Closeup view of inner core. Ribbons are stream traces of the director field, indicating the direction of DNA at various positions within the capsid. Color indicates energy density.	74
4.7	Results of FSA applied to spool configuration on 20-point-per-edge lattice: (a) Full view, (b) Closeup view of inner core. Ribbons are stream traces of the director field, indicating the direction of DNA at various positions within the capsid. Color indicates energy density.	75
4.8	Results of CG applied to spool configuration on 10-point per edge lattice: (a) Full view, (b) Closeup view of inner core. Ribbons are stream traces of the director field, indicating the direction of DNA at various positions within the capsid. Color indicates energy density.	76
4.9	Results of CG applied to spool configuration on 20-point per edge lattice: (a) Full view, (b) Closeup view of inner core. Ribbons are stream traces of the director field, indicating the direction of DNA at various positions within the capsid. Color indicates energy density.	76
B.1	Local stencil for the relaxation iteration.	85

Chapter 1

Introduction

A virus consists essentially of a genome (either RNA or DNA) inside a container composed of proteins. The virus attacks or infects a host cell by releasing its genome inside the cell. The machinery of the host cell then processes the genetic information of the virus and is thereby “hijacked”, and tricked into producing all of the components for new progeny viruses. Once assembly of the protein container or *capsid* of a new virus is complete, the newly replicated genome is threaded inside, segment by segment. This packaging process can be a remarkable feat of confinement. Many bacteriophages (viruses which attack bacteria cells) in particular are able to package their genomes extremely tightly. For instance, whereas the length of the T4 bacteriophage genome is of the order of $54\ \mu\text{m}$, the diameter of the head of the T4 virus is a mere 100 nm (Bloomfield, 1997). Therefore the packaging of the T4 genome entails a 540:1 linear compression ratio. Simply scaling these dimensions to more a tangible size, this is similar to packing 400 feet of quarter-inch electrical extension cord into a (nine-inch-diameter) basketball! Most interesting is the fact that this packaging process involves a delicate balance of forces which are both mechanical and electrostatic in nature. The packing dimensions turn out to be exactly of the scale at which DNA can be considered a mechanically stiff rod. However, this rod has a very large negative total charge to it, such that strong repulsive electrostatic forces are experienced when the DNA is densely packed in the head of a virus.

In recent years, an explosion of single-molecule experiments has made it possible to directly probe and measure forces such as these. As a pertinent example, the force vs. fraction of packaged genome for the *Bacillus subtilis* $\phi 29$ bacteriophage has been measured

through the use of optical tweezers to pull on single DNA molecules as they are packaged (Smith et al., 2001). Similar experiments (e.g., Smith et al., 1992; Strick et al., 1996) have generated a quantitative understanding of the elastic properties of the DNA itself as it undergoes bending and twisting. Quantitative studies have also revealed much about the electrostatic forces experienced by DNA (Rau et al., 1984; Parsegian et al., 1986; Rau and Parsegian, 1992).

Concurrently, structural biologists have made fantastic progress in determining to very high resolution the physical structure of the individual components of cells and viruses. Recently the structure of the portal motor which translocates double-stranded DNA into the head of the *Bacillus subtilis* ϕ 29 bacteriophage has been determined to within 3.2 Å resolution by X-ray crystallography (Simpson et al., 2000). Similarly, techniques of cryo-electron microscopy are making it possible to see with increasing clarity the structural organization of DNA packed within viruses. Recent work by Olson et al. (2001) on the T4 bacteriophage and by Cerritelli et al. (1997) on the T7 bacteriophage certainly attest to this fact.

Of principal interest in the study of viral packing are the details of natural physical arrangements or conformations adopted by DNA as it is packed within viruses. Existing models of the structure of packaged DNA posit *spool*-like geometries (Earnshaw and Harrison, 1977), *toroids* (Hud, 1995) and other geometries (Black et al., 1985). The available observational evidence (Olson et al., 2001; Cerritelli et al., 1997), while somewhat lacking in resolution and therefore inconclusive, lends some credence to the spool structural motif. For instance, cryo-electron microscopy observations of Olson et al. (2001) (see Figure 1.1) reveal that the duplex DNA genome of the T4 bacteriophage forms a highly condensed series of concentric layers, spaced about 2.36 nm apart, that follow the general contour of the inner wall of the protein capsid. In addition, the work of Cerritelli et al. (1997) (see Figure 1.2) suggests that the T7 genome is spooled around the capsid in approximately six coaxial shells in a quasicrystalline packing. Brownian molecular dynamics simulations of DNA packaging based on semi-rigid bead-string representations of the genome with Leonard-Jones bead interactions have been carried out by Kindt et al. (2001).

These remarkable advances in experimental biology provide an adequate empirical foundation for the development of theories and models for the mechanics of DNA pack-

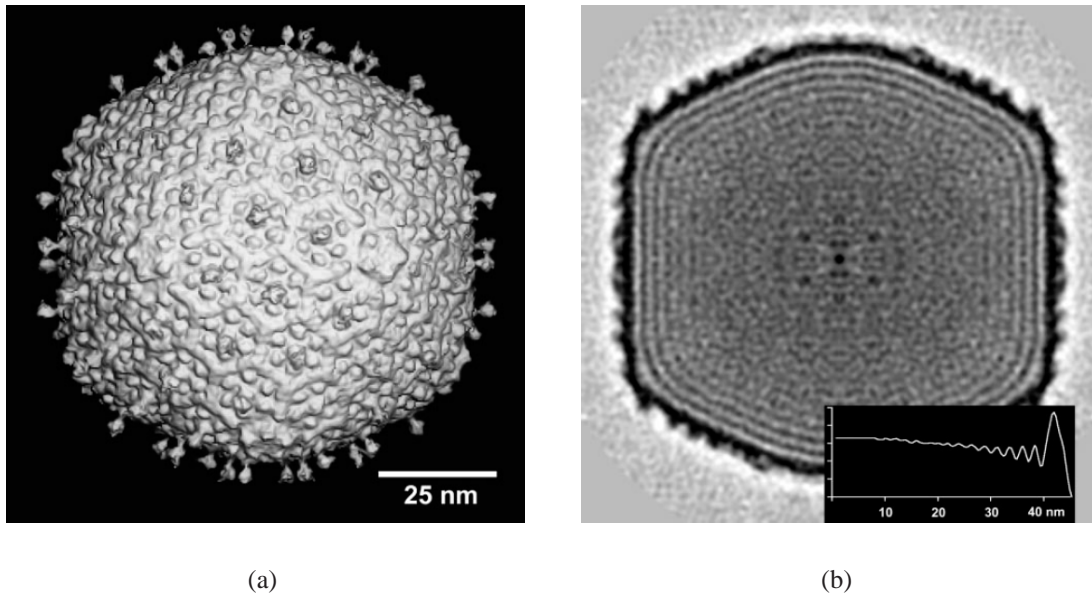


Figure 1.1: Cryo-electron microscopy images of the T4 bacteriophage reprinted from the work of Olson et al. (2001), Copyright 2001, with permission from Elsevier. (a) Shaded-surface rendering of the three-dimensional reconstruction of a filled T4 virus. (b) Central section of the reconstructed T4 density map (high-density features appear dark).

aging in viruses. Notably, Ubbink and Odijk (1996) and Odijk (1998) have developed a mathematical framework for studying the energetics and shapes of DNA condensates both in solution and inside of viruses. Similarly Tzlil et al. (2003) have formed a simple continuum model of viral DNA which draws connections to the study of DNA condensation in solution. Their models have shown the optimal shape of the condensate to evolve continuously from a torus to a spool-like shape. Purohit et al. (2003) have recently described theoretically the mechanics of both the DNA and the capsid. We note that each of these works relies to some degree on the assumption of an axisymmetric motif known as the inverse spool.

The objective of this thesis is the formulation and application of a continuum theory of viral DNA packaging based on a *director-field* representation of the encapsidated DNA. Instead of tracking the DNA segment-by-segment down the strand (a one-dimensional continuum), the director-field approach views the DNA conformations as spatial fields. This representational paradigm affords considerable convenience for purposes of analyz-

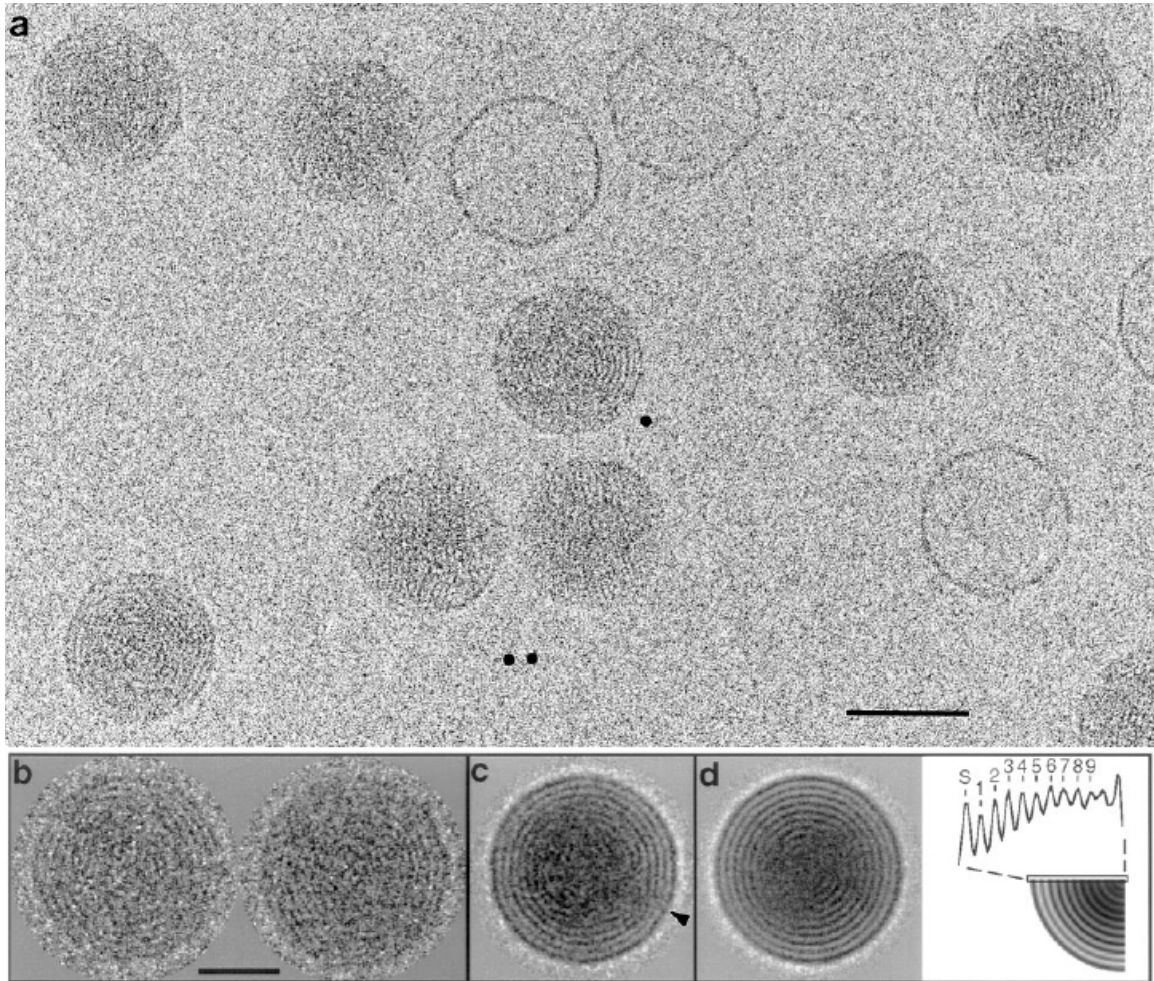


Figure 1.2: Cryo-electron micrograph and computer-processed images of T7 bacteriophage reprinted from the work of Cerritelli et al. (1997), Copyright 1997, with permission from Elsevier. (a) Cryo-electron micrograph of a field of bacteriophage T7 heads. The concentric ring motif is evident in virus viewed along the axis through the portal and the center of the virus (e.g., the virus indexed with a single closed circle). Scale bar = 50 nm. (b) Two axial views at higher magnification. Scale bar = 25 nm. (c and d) Images obtained by averaging 21 and 77 viruses, respectively.

ing complex DNA conformations with a minimum of *a priori* assumptions about their geometry. Chapter 2 sets out this director-field theory in full mathematical detail. The defining property of the director field is that its point values give the local direction and density of the DNA. Thus, the director field supplies a complete description of the DNA conformation, and its determination is the central goal of the theory. The continuity of the DNA strand requires the director field to be divergence-free and tangent to the capsid. The energy of the DNA is defined as a functional of the director field which accounts for bending, torsion, and for electrostatic interactions through a density-dependent interaction energy (Kindt et al., 2001; Tzlil et al., 2003).

The operative principle which determines the DNA conformation is assumed to be *energy minimization*. This principle, together with the complex structure of the energy functional, suggests the use of (i) direct methods of the calculus of variations for the analytical characterization of energy-minimizing conformations, and (ii) methods of global numerical optimization for discretized computational treatment of the problem.

In Chapter 3, we bypass the use of the Euler-Lagrange—or equilibrium—equations of the energy functional and seek to directly formulate *constructions* yielding low-energy conformations of the DNA. For axisymmetric capsids, a simple construction known as the *inverse spool* (Earnshaw and Harrison, 1977) may be evaluated analytically with some generality. We regard the inverse spool as a “baseline” DNA conformation, and subsequent constructions are aimed at successively lowering the energy from that baseline. In particular, we show that under certain restrictions *torsionless toroidal solenoids*, consisting of planar coils contained on meridional planes and wrapped around a spool core, and fine mixtures of the solenoid and spool phase, *beat* the inverse spool construction.

Chapter 4 follows a different strategy, searching for energy minimizing DNA conformations in a discrete space. The director field and all other relevant field quantities are defined at discrete points on a computational lattice. The discrete energy sum approximating the total energy of the DNA is then minimized using *simulated annealing* and the *nonlinear conjugate gradient* method. Numerical results further support the inverse spool hypothesis in general, but reveal additional structure not previously predicted by other theoretical models.

Chapter 2

The Theory

This chapter introduces the field theory upon which the whole of this thesis is based. This theory employs a *director* (a familiar concept in the mechanics of thin structural members) to describe the geometry of the encapsidated DNA.

Over the last 25 years, many researchers (Riemer and Bloomfield, 1978; Ubbink and Odijk, 1996; Tzlil et al., 2003; Purohit et al., 2003, to name just a few) have gained enormous insight and understanding of the mechanics of DNA from a simple hypothesis: DNA as a charged, stiff rod. In the context of viral packing, this hypothesis is routinely supplemented with fairly restrictive assumptions about the geometric configurations adopted by DNA. Such restricted configurations as the inverse spool (stacked concentric hoops of decreasing radius) have been adopted primarily because of the difficulty of tracking individual segments in a more general, complex, unconstrained packing arrangement. Accounting for self-avoidance of the strand and for long-range interactions given a segment-by-segment description of a complex arrangement is an extreme challenge.

In order to circumvent this challenge, we suspend the notion of a DNA strand as a sequence of base pairs, and instead seek to describe the DNA conformations by means of a *director field*. At every point within the capsid, the director field gives the direction and density of DNA. This approach permits the efficient geometrical representation of general, complex DNA arrangements without requiring a detailed accounting of every individual DNA segment. The goal of this chapter is to set out this idea in full mathematical detail.

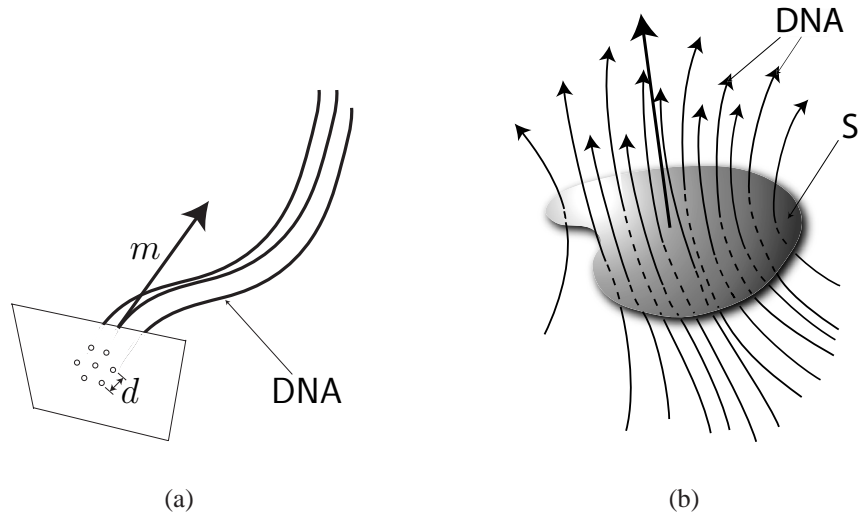


Figure 2.1: a) Director-field representation of the geometry of a DNA condensate. b) Director-field definition in terms of DNA flux through an oriented surface S .

2.1 Director-field description

Consider a simply-connected open bounded subset Ω of \mathbb{R}^3 (the *capsid*), with Lipschitz boundary $\partial\Omega$, containing a self-avoiding inextensible rod (the *DNA*) of length L and small but finite cross section. The axis of the DNA strand traces a curve Γ to which we assign a traversal direction or orientation. The *DNA director field* is a vector field $\mathbf{m} : \Omega \rightarrow \mathbb{R}^3$ with the defining property that, if S is an oriented surface within Ω , possibly with boundary, and ν is the unit normal to S , then

$$N(S) = \int_S \mathbf{m} \cdot \nu \, dS \quad (2.1.1)$$

is the number of signed crossings of Γ through S , Figure 2.1. A crossing is counted as positive if Γ pierces S in the direction of ν , and as negative otherwise. For any closed surface S (containing both or neither of the free ends of the strand), conservation of mass requires that

$$\int_S \mathbf{m} \cdot \nu \, dS = 0, \quad (2.1.2)$$

as the number of inward crossings must equal the number of outward crossings. At points where \mathbf{m} is differentiable this places the constraint

$$\nabla \cdot \mathbf{m} = 0, \quad (2.1.3)$$

i.e., the director field must be divergence-free, whereas on a smooth surface of discontinuity of \mathbf{m} , mass balance requires that

$$[[\mathbf{m}]] \cdot \boldsymbol{\nu} = 0, \quad (2.1.4)$$

where $\boldsymbol{\nu}$ is the local unit normal to the surface of discontinuity and $[[\mathbf{m}]]$ is the corresponding jump of \mathbf{m} .

The local DNA-length density per unit volume is given by the scalar field $|\mathbf{m}|$. This field has the property that, for any subset $U \subset \Omega$,

$$L(U) = \int_U |\mathbf{m}| dx \quad (2.1.5)$$

is the length of the DNA contained within U . In particular, $|\mathbf{m}| = 0$ in regions not filled by DNA, and the total length of DNA within the capsid is

$$L = \int_{\Omega} |\mathbf{m}| dx. \quad (2.1.6)$$

Borrowing jargon from the study of DNA condensation, we refer to this mass of DNA within the capsid (i.e., the region in which $|\mathbf{m}| > 0$) as the *condensate*.

The unit vector field

$$\mathbf{t} = \frac{\mathbf{m}}{|\mathbf{m}|} \quad (2.1.7)$$

gives the local unit tangent to the DNA. The Serret-Frenet orthonormal triad at every point of the DNA is completed by the normal vector \mathbf{n} and the binormal vector \mathbf{b} . These vectors are related by the Serret-Frenet formulae

$$\mathbf{t}' = \kappa \mathbf{n}, \quad \mathbf{n}' = \tau \mathbf{b} - \kappa \mathbf{t}, \quad \mathbf{b}' = -\tau \mathbf{n}, \quad (2.1.8)$$

where κ is the curvature and τ is the torsion. Here and subsequently a prime denotes the arc-length derivative in the direction of \mathbf{t} , i.e.,

$$f' = \mathbf{t} \cdot \nabla f \quad (2.1.9)$$

for any function f defined over Ω . It follows from (2.1.8) that

$$\kappa^2 = |\mathbf{t}'|^2, \quad (2.1.10a)$$

and

$$\tau^2 = |\mathbf{n}' + \kappa \mathbf{t}|^2 = |\mathbf{n}'|^2 - \kappa^2 = \frac{\mathbf{t}'' \cdot \mathbf{P}(\mathbf{t}') \cdot \mathbf{t}''}{|\mathbf{t}'|^2} - |\mathbf{t}'|^2, \quad (2.1.10b)$$

where $\mathbf{P}(\mathbf{a}) \equiv \mathbf{I} - \mathbf{a} \otimes \mathbf{a}/|\mathbf{a}|^2$ is the orthogonal projection in the direction of a vector $\mathbf{a} \in \mathbb{R}^3$. Insertion of (2.1.7) into (2.1.10) yields κ^2 and τ^2 in terms of the DNA density field \mathbf{m} . We note that, conveniently, neither κ^2 nor τ^2 requires the introduction of a specific sign convention for the curvature or the torsion of a curve.

2.2 Energetics of packaged DNA

The working assumption underlying the present work is that the conformations adopted by viral DNA are, or are close to, energy minimizers. This variational principle can be connected to the second law of thermodynamics by considering the *free energy*, $U - TS$ (with U = internal energy, T = temperature, and S = entropy). Statistical mechanics would understand a free-energy minimizer consistent with all physical constraints to be the most probable state for the system. We therefore proceed to assign an appropriate free energy to the director field and, subsequently, we endeavor to characterize its minimizers.

The energetics of viral DNA is the result of a complex array of factors (Riemer and Bloomfield, 1978; Bloomfield, 1996, 1997; Kindt et al., 2001; Tzlil et al., 2003), including entropy reduction associated with confinement to the capsid; stretching, bending and torsion; and electrostatic interactions. Riemer and Bloomfield (Riemer and Bloomfield, 1978)

estimated the entropic effect of confinement and found it to be negligibly small in comparison to the other effects. The elastic strain energy due to bending and torsion may be estimated by means of conventional rod theory (e.g., Antman, 1995). Following Kindt et al. (Kindt et al., 2001; Tzilil et al., 2003) and Purohit et al. (Purohit et al., 2003), the net effect of all electrostatic interactions may be accounted for by means of an density-dependent effective *interaction energy*, also sometimes referred to as a *cohesive energy*. In this section, each of these energies is considered in turn and expressed in terms of the director field \mathbf{m} .

2.2.1 Elastic energy

We choose to model the mechanical behavior of DNA via the theory of (geometrically nonlinear) elastic rods. The local strain-energy per unit volume of DNA due to bending and torsion is (e.g., Antman, 1995)

$$W(\mathbf{m}, \nabla \mathbf{m}, \nabla \nabla \mathbf{m}) = \left\{ \frac{A}{2} \kappa^2 + \frac{B}{2} \tau^2 \right\} |\mathbf{m}|, \quad (2.2.1)$$

where A and B are the bending and torsional stiffnesses, respectively, κ is the local curvature (2.1.10a) and τ is the local torsion (2.1.10b). Recent experiments on single DNA molecules have made it possible to measure directly force-deformation behavior of DNA helices (Smith et al., 1992, 2001). “Wormlike chain” models have been successful at predicting this behavior based on a fitting parameter known as the *persistence length*. Entropic in nature, the bending and torsional stiffnesses of DNA are of the form $A = ak_B T$, and $B = bk_B T$, respectively, where T is the absolute temperature, $k_B = 1.38 \times 10^{-23} \text{ J/K}$ is Boltzmann’s constant, a is the *bend persistence length* and b is the *twist persistence length*. Physically, a persistence length measures the length of DNA for which the end point directions are statistically uncorrelated (Boal, 2002). So, clearly, a shorter persistence length corresponds to a more flexible molecule, and conversely a longer persistence length means greater stiffness. The bend persistence length of DNA is widely acknowledged to be $a \approx 50$ nm. There is less consensus about the value of the torsion persistence length, which has been reported in the general range $50 \text{ nm} < b < 120 \text{ nm}$. For the present work, we choose $b = 85$ nm, a value which is representative of some recent predictions (Moroz and Nelson,

1998; Bouchiat and Mezard, 2000).

2.2.2 Interaction energy

DNA is a highly charged polymer, with one negative charge for every 0.17 nm of its length (Gelbart et al., 2000). Given the tight spacing inside the viral capsid, some account must be made for the electrostatic interactions resulting from this high charge. According to experiments using osmotic pressure techniques (Parsegian et al., 1986; Rau et al., 1984; Rau and Parsegian, 1992), at small interaxial separation distances the dominant interaction forces experienced by DNA are described as “hydration forces” arising from the work related to the reconfiguring of water molecules in the surrounding solution. Depending on the interaxial spacing and composition of the solution, these hydration forces can be either repulsive or attractive. Nevertheless, as we will show, potential energies describing both of these behaviors can be modeled with the same functional form.

Repulsive interaction. Parsegian et al. (1986) and Rau et al. (1984) characterized the repulsive “hydration” forces acting on DNA double helices condensed by exposure to the polymer polyethyleneglycol (PEG) in solution. Measurements were made correlating the compressing osmotic pressure of DNA packed in a hexagonal lattice with the interaxial spacing of the lattice. The dependence of pressure P on spacing d was found to be exponential, i.e.,

$$P(d) = F_0 e^{-d/c} \quad (2.2.2)$$

with a decay distance c in the range 2.5–3.5 Å.

Denote by $u = |\mathbf{m}|$ the DNA length density per unit volume. Then for a hexagonally packed array the relationship between density and interaxial spacing is

$$u = \frac{2}{\sqrt{3}d^2}. \quad (2.2.3)$$

As has been done by Kindt et al. (2001), Tzllil et al. (2003), and Purohit et al. (2003), we can compute the work required to bring the DNA helices in a unit cell of the hexagonal

array together from infinite separation to a spacing d by integration. The interaction energy per unit volume DNA can be computed from the opposite of this work:

$$\begin{aligned}\phi(u) &= -u \int_{\infty}^{d=\sqrt{\frac{2}{\sqrt{3}u}}} P(\xi) \sqrt{3} \xi d\xi \\ &= \frac{F_0}{2} \left(\frac{u}{u_\infty} + \sqrt{\frac{u}{u_\infty}} \right) e^{-\sqrt{u_\infty/u}},\end{aligned}\tag{2.2.4}$$

where $u_\infty = \frac{2}{\sqrt{3}c^2}$. The repulsive interaction potential $\phi(u)$ is shown in Figure 2.2.

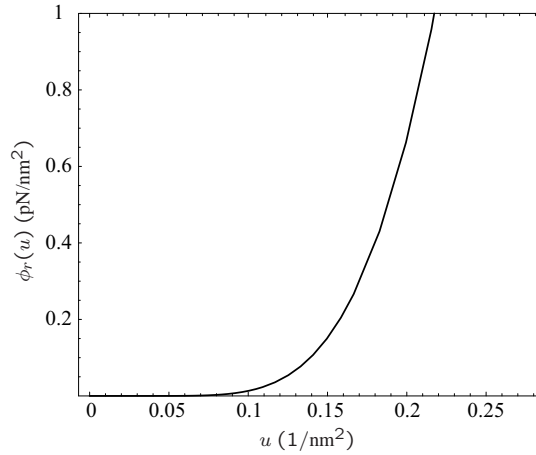


Figure 2.2: Repulsive interaction potential. $F_0 = 55000$ pN/nm² and $c = 0.28$ nm.

Net-attractive interaction. When the solution surrounding the DNA contains a sufficient concentration of polyvalent cations (trivalent, tetravalent, or greater valence), the DNA self-organizes into coiled condensates in the shape of toroids. X-ray diffraction shows that the DNA in these toroids is packed in a hexagonal lattice of double-stranded helices (Rau and Parsegian, 1992). With experimental techniques similar to those mentioned above for the repulsive case, measurements were made (Rau and Parsegian, 1992) of the relationship between osmotic pressure applied to the DNA lattice and interaxial spacing. Evidence was shown of attractive hydration forces that cause the DNA to maintain a “preferred” spacing, $d_0 \approx 28$ Å, which depends slightly on the type of condensing ligand introduced into solution. Hydration forces are again repulsive at small spacings, as evidenced by osmotic pressure measurements, and a clear equilibrium is observed at the preferred spacing. Kindt

et al. (2001) and Tzlil et al. (2003) suggested an exponential fit of the pressure-spacing results of Rau and Parsegian (1992) in the form

$$P(d) = F_0 \{e^{-(d-d_0)/c} - 1\}, \quad (2.2.5)$$

where the decay distance is now $c \approx 1.4 \text{ \AA}$. Again an interaction energy per unit length is computed by integration

$$\begin{aligned} \phi(u) &= e_0 u + u\sqrt{3} \int_{d=\frac{2}{\sqrt{3}u}}^{d_0} P(\xi)\xi d\xi \\ &= \phi_0 - \mu_0 u + (\mu_0 + \mu_\infty)(u + \sqrt{u_\infty u})e^{-\sqrt{u_\infty/u}} \end{aligned} \quad (2.2.6)$$

where we write

$$\phi_0 = F_0 \quad (2.2.7a)$$

$$u_\infty = \frac{2}{\sqrt{3}c^2} \quad (2.2.7b)$$

$$\mu_0 = \frac{\sqrt{3}}{2}\phi_0(2c^2 + 2cd_0 + d_0^2) - e_0 \quad (2.2.7c)$$

$$\mu_\infty = \sqrt{3}\phi_0 c^2 e^{d_0/c} - \mu_0. \quad (2.2.7d)$$

This net-attractive interaction potential is shown in Figure 2.3. By inspection of Figure 2.3, it is evident that $\phi(u)$ is a convex function of u which attains a minimum near $u_0 = (2/\sqrt{3})/d_0^2 = 0.147 \text{ nm}^{-2} = 2.87 \times 10^{-3}u_\infty$. It should be carefully noted, however, that the function $\phi(|\mathbf{m}|)$ is a *nonconvex* function of \mathbf{m} , a property which may be expected to promote the formation of complex DNA structures.

Note also that the $\phi_a(u)$ has two qualitatively distinct regions of behavior: (i) the attractive region, where u is smaller than $u_0 = (2/\sqrt{3})/d_0^2$, and where $\phi_a(u)$ is ostensibly linear; and (ii) in the repulsive region, where u is greater than u_0 , and where $\phi_a(u)$ shows a steep upward turn. Considering this qualitative behavior and the corresponding asymptotic behavior of the functional form, a simple approximate model is derived below.

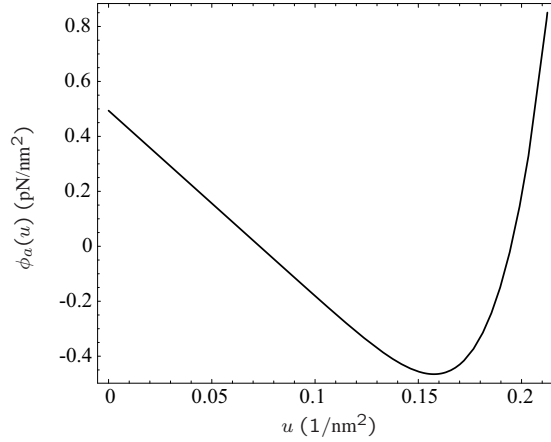


Figure 2.3: Attractive interaction potential. $e_0 = 0.12k_B T/\text{nm}$, $\phi_0 = 0.12k_B T/\text{nm}^2$ and $c = 0.28 \text{ nm}$.

Note also, that by simply adjusting the constants of (2.2.7) to,

$$\phi_0 = 0 \quad (2.2.8a)$$

$$u_\infty = \frac{2}{\sqrt{3}c^2} \quad (2.2.8b)$$

$$\mu_0 = 0 \quad (2.2.8c)$$

$$\mu_\infty = \frac{F_0}{2u_\infty}, \quad (2.2.8d)$$

the repulsive potential Eq. (2.2.4) is shown to be a special case of the attractive potential Eq. (2.2.6). Thus, henceforth we will only refer to Eq. (2.2.6) as the general interaction potential or cohesive energy.

Approximate model of net-attractive interaction. The chemical potential follows as

$$\mu \equiv \partial\phi(u) = -\mu_0 + (\mu_0 + \mu_\infty)e^{-\sqrt{u_\infty/u}} \left(1 + \sqrt{\frac{u_\infty}{u}} + \frac{1}{2} \frac{u_\infty}{u} \right), \quad (2.2.9)$$

where, here and subsequently, the operator ∂ denotes the ordinary derivative of a differentiable function, or the subdifferential of a general convex function (Rockafellar, 1970), possibly non-smooth, as the case may be. As will become apparent in the sequel, the dual

of the cohesive energy function (Rockafellar, 1970),

$$\phi^*(\mu) = \sup_u \{\mu u - \phi(u)\} = - \inf_u \{\phi(u) - \mu u\}, \quad (2.2.10)$$

provides a useful device for understanding certain energy minimizing DNA conformations such as the inverse spool. The dual cohesive energy corresponding to (2.2.6) is depicted in Figure 2.4. The convexity of $\phi^*(\mu)$, which is evident in this figure, is a direct consequence of the convexity of $\phi(u)$. From general convex analysis (Rockafellar, 1970) it follows that

$$u = \partial\phi^*(\mu), \quad (2.2.11)$$

i.e., the dual cohesive energy $\phi^*(\mu)$ acts as a potential for the inverse of the chemical potential vs. density relation (2.2.9).

The general structure of the energy functions (2.2.6) and (2.2.10) is noteworthy. Thus, the function $\exp(-\sqrt{u_\infty/u})$ and all its derivatives vanish at $u = 0$, and, consequently, in the regime $u \ll u_\infty$ one has asymptotically

$$\phi(u) \sim \phi_0 - \mu_0 u. \quad (2.2.12)$$

By contrast, in the regime $u \gg u_\infty$ the function $\exp(-\sqrt{u_\infty/u})$ approaches 1 asymptotically and, consequently, we have

$$\phi(u) \sim \phi_\infty + \mu_\infty u, \quad (2.2.13)$$

where

$$\phi_\infty = \phi_0 - \frac{1}{2}(\mu_0 + \mu_\infty)u_\infty. \quad (2.2.14)$$

The asymptotic behavior (2.2.12) is clearly apparent in Figure 2.3. Thus, $\phi(u)$ is ostensibly linear for small u , and subsequently attains a minimum at u_0 followed by a sharp upturn. The high-density linear asymptotic behavior (2.2.13) is eventually approached, but only for densities of the order of u_∞ , i.e., two orders of magnitude larger than u_0 . Correspondingly, the chemical potential μ remains nearly constant at $-\mu_0$ for small u and grows to the much

larger asymptotic value μ_∞ rapidly thereafter. Thus, for $\mu < -\mu_0$ and $|\mu| \gg \mu_0$ one has

$$\phi^*(\mu) \sim -\phi_0, \quad (2.2.15)$$

whereas for $\mu > -\mu_0$ and $|\mu| \gg \mu_0$ we find

$$\phi^*(\mu) \sim -\phi_0 + (\mu_0 + \mu) \frac{u_\infty}{2}. \quad (2.2.16)$$

These two regimes are clearly evident in Figure 2.4.

The essence of the behavior just described is captured by a particularly simple cohesive energy. Thus, we expect the cohesive energy to decrease linearly from ϕ_0 for small u . Additionally, in view of the subsequent sharp upturn of the energy, and provided that the chemical potential remains at moderate values not much larger than μ_0 , we expect the density of the DNA condensate to remain close to the preferred density u_0 . The simplest functions which deliver this behavior are

$$\phi(u) = \begin{cases} \phi_0 - \mu_0 u, & \text{if } u \leq u_0, \\ +\infty, & \text{otherwise,} \end{cases} \quad (2.2.17)$$

and

$$\phi^*(\mu) = \begin{cases} -\phi_0, & \text{if } \mu \leq -\mu_0, \\ -\phi_0 + (\mu + \mu_0)u_0, & \text{otherwise,} \end{cases} \quad (2.2.18)$$

which in turn give the relations

$$\begin{aligned} \mu(u) &= -\mu_0, & \text{if } u < u_0, \\ \mu(u) &\geq 0, & \text{if } u = u_0, \end{aligned} \quad (2.2.19)$$

and

$$u(\mu) = \begin{cases} 0, & \text{if } \mu \leq -\mu_0, \\ u_0, & \text{otherwise.} \end{cases} \quad (2.2.20)$$

It is evident from these relations that the corresponding DNA conformations may comprise

a dilute phase, at density $u = 0$, in regions where the chemical potential is strictly smaller than $-\mu_0$; a fully dense phase, at density u_0 , in regions where the chemical potential is strictly greater than $-\mu_0$; and a mixed phase, at intermediate densities $0 \leq u \leq u_0$, in regions where the chemical potential is exactly equal to $-\mu_0$.

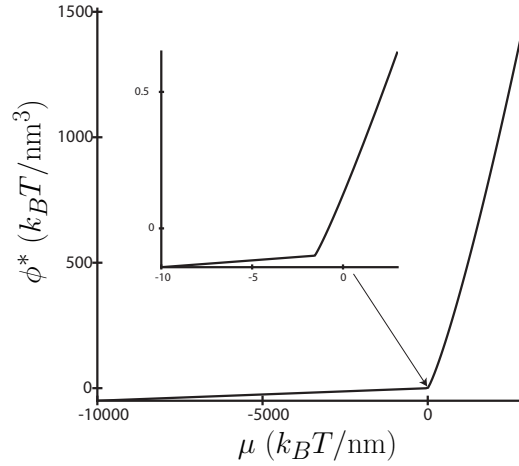


Figure 2.4: Dual of attractive DNA interaction energy function vs. chemical potential.

Surface energy. Recall that the interaction energy models above assume that DNA helices are packed in a hexagonal lattice, and with the approximate energy (2.2.17) enacted, the spacing of that lattice is constant, as stated by (2.2.20). However, we might hypothesize a model where the helices are packed in a lattice (either constant-spaced or not) with a boundary across which the DNA density u jumps from some nonzero value \bar{u} to 0. Helices on the boundary of a condensate have fewer neighbor helices than helices in the interior, and thus they experience different interaction forces.

Consider an arc-length ℓ of DNA in a hexagonal array of density u . The total interaction energy associated with that arc-length is $\phi(u)\ell/u$. Creating a boundary surface adjacent to this piece of DNA involves breaking the interactions with a few of its 6 neighbors (most likely 2 or 3, depending of geometry of the boundary surface). The change in the strand's

energy produced by breaking these interactions is

$$\Delta e = -\phi(u) \frac{\ell n}{u 6}$$

(where n is the number of broken neighbor interactions). The total surface area attributed to the arc-length is $A = d\ell$. Thus, the surface energy density per unit area is

$$\gamma(u) \equiv \frac{-\phi(u) n}{ud(u) 6} = \frac{-\phi(u) n}{\sqrt{2u/\sqrt{3}} 6}, \quad (2.2.21)$$

where, of course, $d(u)$ is given by the inverse of equation (2.2.3), namely, $d(u) = \sqrt{2/(\sqrt{3}u)}$. The number of broken neighbor interactions should depend, in general, on the geometry (namely the curvature) of the boundary interface. However, for simplicity, we assume $n = 3$. This form of the surface energy is identical to that which was proposed by Kindt et al. (2001).

2.2.3 Total energy and variational problem

The total free energy of the DNA (neglecting surface effects for the moment) is now the sum of its strain and cohesive energies, namely,

$$E(\mathbf{m}) = \int_{\Omega} [W(\mathbf{m}, \nabla \mathbf{m}, \nabla \nabla \mathbf{m}) + \phi(|\mathbf{m}|)] dx. \quad (2.2.22)$$

As previously stated, the presumed operative principle is energy minimization, and thus we expect that the DNA will adopt such conformations as minimize its energy. This process of energy minimization is subject to the divergence constraint (2.1.3); in addition, the DNA must be tangent to the boundary $\partial\Omega$ of the capsid. In conclusion, the optimal packaging arrangement of a length L of DNA inside a capsid Ω follows from the minimization problem:

$$\inf E(\mathbf{m}), \quad (2.2.23a)$$

$$\text{subject to: } \nabla \cdot \mathbf{m} = 0 \quad \text{in } \Omega, \quad (2.2.23b)$$

$$\mathbf{m} \cdot \boldsymbol{\nu} = 0 \quad \text{on } \partial\Omega, \quad (2.2.23c)$$

$$\int_{\Omega} |\mathbf{m}| dx = L, \quad (2.2.23d)$$

where $\boldsymbol{\nu}$ is the outward unit normal to $\partial\Omega$ and we have made use of identity (2.1.6). The force exerted on the portal by the packaged DNA is

$$F = \frac{dE(L)}{dL} \equiv F(L), \quad (2.2.24)$$

where $E(L)$ is the infimum of the energy functional $E(\mathbf{m})$ for given length L of genome packaged. Of course, this force should not be directly construed as the force which needs to be imparted by the portal motor in order to package additional DNA. Indeed, the total energy of the genome is

$$E^{\text{tot}}(L) = E(L) + E^{\text{ext}}(L_0 - L), \quad (2.2.25)$$

where L_0 is the total length of the genome, and $E^{\text{ext}}(L_0 - L)$ is the energy of the external DNA lying outside the capsid. The total packaging force is, therefore

$$F^{\text{tot}}(L) = \frac{dE^{\text{tot}}(L)}{dL}. \quad (2.2.26)$$

If, for instance, the external DNA forms a condensate, then E^{ext} may be expected to be a decreasing function of the external length $L - L_0$, and the deconstruction of the condensate requires an additional force that needs to be supplied by the portal motor.

A simple special case of problem (2.2.23) concerns the determination of the DNA arrangement after the entire genome is packaged. If, in addition, the cohesive energy is assumed to be of the form (2.2.17), the DNA density may be taken to be $u = u_0$ everywhere

inside the capsid, the length of DNA is

$$L_0 = |\Omega|u_0, \quad (2.2.27)$$

and the problem reduces to determination of the unit director field \mathbf{t} , Eq. (2.1.7). Specifically, the variational problem is

$$\inf E(\mathbf{t}), \quad \text{subject to: } \begin{cases} \nabla \cdot \mathbf{t} = 0 & \text{and } |\mathbf{t}| = 1, & \text{in } \Omega, \\ \mathbf{t} \cdot \boldsymbol{\nu} = 0, & & \text{on } \partial\Omega, \end{cases} \quad (2.2.28)$$

where the energy functional is now

$$E(\mathbf{t}) = \int_{\Omega} \left\{ \frac{A}{2} \kappa^2 + \frac{B}{2} \tau^2 \right\} u_0 dx. \quad (2.2.29)$$

The structure of problem (2.2.28) bears some resemblance to problems in micromagnetics (see, e.g., de Simone et al., 2000, for a recent review), where divergence and modulus constraints such as those in (2.2.28) arise naturally. We note, in particular, that the modulus constraint is *nonconvex*.

As a final case, consider the situation posed at the end of the previous section, in which the density field makes a jump across the condensate boundary $\partial\bar{\Omega}$. In this case, a surface term is necessarily added to the total energy to yield

$$E(\mathbf{m}, \partial\bar{\Omega}) = \int_{\Omega} [W(\mathbf{m}, \nabla\mathbf{m}, \nabla\nabla\mathbf{m}) + \phi(|\mathbf{m}|)] dx + \int_{\partial\bar{\Omega}} \gamma(|\mathbf{m}|) dA \quad (2.2.30)$$

if the full interaction energy (2.2.6) is used, or

$$E(\mathbf{t}, \partial\bar{\Omega}) = \int_{\Omega} \left\{ \frac{A}{2} \kappa^2 + \frac{B}{2} \tau^2 \right\} u_0 dx + \int_{\partial\bar{\Omega}} \gamma(u_0) dA \quad (2.2.31)$$

if the approximate interaction energy (2.2.17) is used. In either case, the total free energy functional is to be minimized with respect to the director field \mathbf{m} and the condensate boundary $\partial\bar{\Omega}$ which are both unknown in general.

2.3 Summary

This chapter has detailed the construction of a director-field theory for modeling of the packaging of DNA into bacteriophage capsids. The director field has been defined as a vector field which gives, as its point values, the local direction and density (length per unit volume) of DNA within the capsid. We have shown how the director field enables a complete geometrical description of the DNA, and we have defined all geometric quantities of interest (total length L , curvature κ , and torsion τ) in terms of the director field. As also shown, the director field is subject to certain constraints, the most essential being the vanishing of its divergence.

We have formed a total free energy functional, defining in detail the appropriate contributions of elasticity and electrostatic interactions completely in terms of the director field. The electrostatic interactions require particular attention, as they vary in nature depending on the chemical constituents of the DNA's solution environment. For this purpose, we have rephrased (in terms of the DNA director field) theoretical models of the electrostatic interactions connected to the osmotic pressure experiments of Rau, Parsegian, and other workers. These models predict behavior which can be either repulsive or attractive depending on chemical environment and external forcing. As well, we have examined simplification/approximation of these models, and extensions of them for consideration of surface effects.

Finally, with the director-field description of the geometry and energetics in place, we have posed several variants of the energy minimization problem, which will be the guiding principle in the chapters to follow. We note again that for each variant of the minimization problem either the energy density or a director field constraint is *nonconvex*. The resulting lack of lower semicontinuity in the free energy functional foreshadows the appearance of “microstructured” solutions, and generally implies an exceedingly complex, multiple-well energy landscape.

Minimization of the free energy functional is the topic of the next two chapters. Conceded by the complex structure of this functional, we avoid classical variational methods involving the functional's Euler-Lagrange—or equilibrium—equations in favor of direct

methods of the calculus of variations. In Chapter 3 we seek to directly formulate analytical *constructions* yielding low-energy conformations of the DNA. In Chapter 4 we hunt for approximate low-energy configurations by discretizing the problem on a finite-difference grid, and performing numerical optimization with *simulated annealing* and the *nonlinear conjugate gradient* method.

Chapter 3

Constructions

As remarked in Chapter 2, the nonconvex nature of the integrands and constraints produced by the director-field theory make it desirable to approach the minimization problem from the perspective of direct methods in the calculus of variations. Thus, this chapter concerns the direct identification and exploration of low-energy DNA conformations which we will call *constructions*.

Over the years, biophysicists have conjectured many possible conformations for the packaged DNA, including the ball and string model (Richards et al., 1973), the inverse spool model (Earnshaw and Harrison, 1977), the spiral-fold model (Black et al., 1985), constant-radius-of-curvature torii (Hud et al., 1995), and bi-folded torii (Hud, 1995). Of these, the spool model appears to be the most popular. The attractiveness of the spool model has been affirmed particularly by recent, very suggestive cryo-electron-micrographs (Cerritelli et al., 1997). Thus, we are motivated to study the spool model in some detail in Section 3.1. With the insight gained from study of the inverse spool, we proceed to propose and investigate a novel construction, the *torsionless toroidal solenoid*, which is inspired by some of the perceived shortcomings of the inverse spool. Finally, we combine the two constructions to form solenoid/spool mixtures. As we show, the solenoid, and subsequently the solenoid/spool mixtures, are able to attain consecutively lower total energies than the simple spool model.

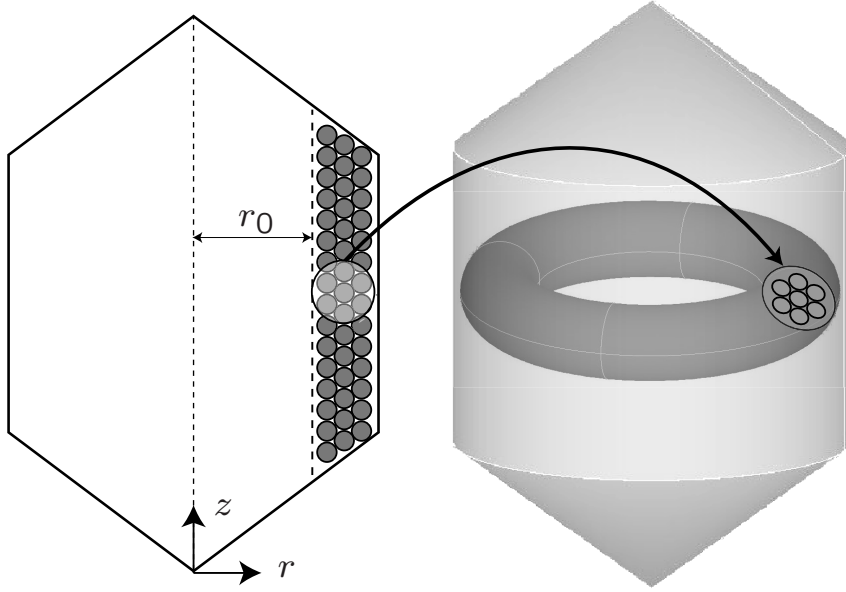


Figure 3.1: Geometry of the inverse-spool conformation.

3.1 Inverse spool construction

For axisymmetric capsids, a simple DNA arrangement known as the *inverse spool* (Earnshaw and Harrison, 1977; Purohit et al., 2003), depicted in Figure 3.1, may be treated analytically with some generality. In the following sections we shall regard the inverse spool as a “baseline” conformation, and subsequent constructions will be aimed at successively lowering the energy from that baseline.

Consider a cylindrical coordinate system (r, θ, z) such that the z -axis is aligned with the axis of the virus. Let R be the maximum of r over Ω , and let $z = a(r)$ and $z = b(r)$, $r \in [0, R]$ define the boundary $\partial\Omega$ of the capsid. Suppose that

$$\mathbf{m} = u(r, z)\mathbf{e}_\theta, \quad (3.1.1)$$

where $\mathbf{e}_\theta(r, \theta, z)$ is the unit circumferential basis vector.¹ By this choice of test director

¹Strictly speaking, the curve traced out by a single DNA strand wrapped in an inverse spool (viewing the strand as a one-dimensional continuum, i.e., a rod) would have to have some nonzero pitch and radial component at various points in space. However, these are clearly negligible, and thus omitted for simplicity in the present model.

fields, the divergence constraint (2.2.23b) and the boundary condition (2.2.23c) are satisfied identically. In addition, the torsion vanishes identically everywhere, the curvature is given by $\kappa^2 = 1/r^2$, and the strain energy density is given by $W(r, u) = Au/(2r^2)$. Finally, the energy (2.2.22) reduces to the simple form

$$E(u) = 2\pi \int_{a(r)}^{b(r)} \int_0^R \left\{ \frac{Au}{2r^2} + \phi(u) \right\} r dr dz. \quad (3.1.2)$$

The length constraint (2.2.23d) may conveniently be enforced by the introduction of the internal force F as a Lagrange multiplier, leading to the Lagrangian

$$I(u, F) = 2\pi \int_{a(r)}^{b(r)} \int_0^R \left\{ \frac{Au}{2r^2} + \phi(u) - Fu \right\} r dr dz. \quad (3.1.3)$$

The minimization $I(u, F)$ with respect to u may now be effected point-wise. In view of (2.2.10), this minimization gives

$$E^*(F) = - \inf_u I(u, F) = 2\pi \int_{a(r)}^{b(r)} \int_0^R \phi^* \left(F - \frac{A}{2r^2} \right) r dr dz, \quad (3.1.4)$$

with the density field given by

$$u(r, z) = \partial \phi^* \left(F - \frac{A}{2r^2} \right). \quad (3.1.5)$$

It is interesting to note that the optimal density distribution (3.1.5) depends on L and is not uniform, although it is a function of r only. Likewise, the integrand in (3.1.4) is independent of z , and, hence,

$$E^*(F) = 2\pi \int_0^R \phi^* \left(F - \frac{A}{2r^2} \right) h(r) r dr, \quad (3.1.6)$$

where we write $h(r) = b(r) - a(r)$. Finally, the minimum energy among all conformations of the form (3.1.1) follows explicitly as

$$E(L) = \sup_F \{ FL - E^*(F) \}. \quad (3.1.7)$$

The Euler-Lagrange equation corresponding to this maximum problem is

$$L = 2\pi \int_0^R \partial\phi^* \left(F - \frac{A}{2r^2} \right) h(r)rdr, \quad (3.1.8)$$

which effectively yields the inverse of relation (2.2.24).

Simple explicit formulae can be obtained for the simplified cohesive energy (2.2.17). In this case, (3.1.8) reduces to

$$L = 2\pi u_0 \int_{r_0}^R h(r)rdr, \quad (3.1.9)$$

where, in view of (2.2.20), the internal radius r_0 of the inverse spool follows from the condition $\mu = -\mu_0$, or

$$F - \frac{A}{2r_0} = -\mu_0, \quad (3.1.10)$$

which yields

$$r_0 = \sqrt{\frac{A}{2(F + \mu_0)}}. \quad (3.1.11)$$

3.1.1 Application to the $\phi 29$ bacteriophage

If, by way of example, Ω is taken to be a capped cylinder, which roughly approximates the geometry of a $\phi 29$ bacteriophage, then

$$h(r) = \left(1 - \frac{r}{R}\right) h_0 + \frac{r}{R} h_R, \quad (3.1.12)$$

and (3.1.9) evaluates to

$$\frac{L}{L_0} = 1 + \frac{1}{2} \frac{1}{(h_0 + 2h_R)R^3} \frac{A}{F + \mu_0} \left[(h_0 - h_R) \sqrt{\frac{2A}{F + \mu_0}} - 3h_0R \right], \quad (3.1.13)$$

where

$$L_0 = \frac{\pi}{3} u_0 (h_0 + 2h_R) R^2 \quad (3.1.14)$$

is the length of the genome.

Evaluation of these formulae is not quite as simple for the full interaction energy (2.2.6), but is nonetheless straightforward. Recall that the density is given by Equation (3.1.5), or equivalently, as the solution to the equation

$$\mu \equiv \partial\phi(u) = F - \frac{A}{2r^2}. \quad (3.1.15)$$

Of course, since $\phi(u)$ is smooth, $\partial\phi(u)$ represents the ordinary derivative of $\phi(u)$, and Equation (3.1.15) is a simple (though nonlinear and transcendental) algebraic equation, which can be solved numerically for the density as a function of position and parameterized by force, $u(r; F)$.

As an example, consider the case when the interaction potential (2.2.6) has a purely repulsive character, with constants satisfying Eqs. (2.2.8). Solving (3.1.15) for the DNA density $u(r; F)$ over a range of F and r yields the contour and surface plots shown in Figure 3.2. Figure 3.3 shows the density and corresponding interaxial spacing first as they vary with force at the maximum radius, and second as they vary with radius at maximum force. From these plots it is clear that the packing rate is highest at lower force values and decreases steadily as force increases (and as more DNA has been packed). It is also clear that at a given force, the density distribution is relatively flat across the virus. However, there is some structure to the density profile at small radius, as the density quickly drops off to zero at a certain radius, leaving an inner core empty. Figure 3.3c shows that this inner core radius is predicted to be about 2 nm when the genome is fully packaged.

Given this solution for the density field, Equation (3.1.8) is evaluated to produce Figure 3.4, which shows the dependence of the internal resistance force on the fraction L/L_0 of packaged genome. Superimposed over this prediction is the experimentally measured dependence reported by Smith et al. (2001). The recent experiments of Smith et al. (2001), measuring the force *vs.* length of packed DNA in the $\phi 29$ bacteriophage were performed in a solution of 50 mM Tris-HCL buffer (pH 7.8), 50 mM NaCl, 5 mM MgCl₂. In this solution, the DNA helices will exhibit the purely repulsive behavior described by (2.2.8). We note, however, that the experiments of Parsegian et al. (1986) and Rau et al. (1984) (from which Eqs. (2.2.8) originate) are in 500 mM NaCl. Therefore, it is reasonable to expect

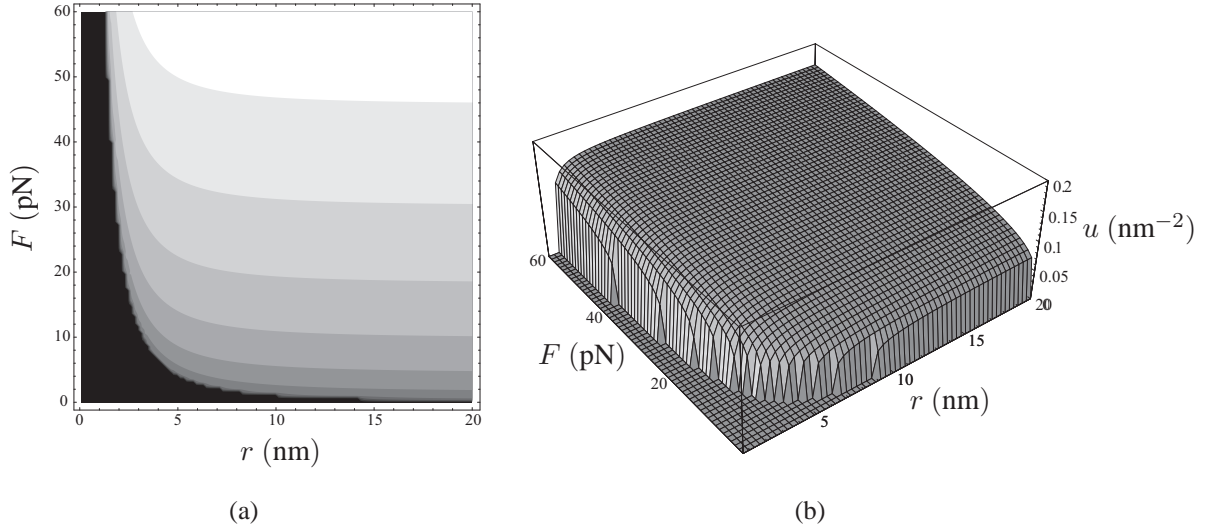


Figure 3.2: Density $u(r, F)$ for a $\phi 29$ capsid with fully repulsive potential: $F \in [0, 60 \text{ pN}]$ and $r \in [0, 21 \text{ nm}]$. a) Contour plot; dark indicates low density, light indicates high density. b) 3-D surface plot.

that the parameter F_0 (and hence μ_∞) might differ for the Smith solution. Constructing the inverse spool using this purely repulsive interaction potential and varying the parameter F_0 to fit the Smith data, we see that $F_0 \approx 4 \times 55000 \text{ pN/nm}^2$ produces a very good fit. The precise values of constants used are shown in Table 3.1. The value of u_∞ corresponds to measurements reported by Rau et al. (1984) and Parsegian et al. (1986). The predictions of the present theory are consistent with the findings of Kindt et al. (2001) and Purohit et al. (2003).

R (nm)	h_0 (nm)	h_R (nm)	A (pN \times nm ²)	μ_∞ (pN)	u_∞ nm ⁻²
21.00	54.00	27.00	202.31	1.758×10^4	12.83

Table 3.1: Assumed constants for $\phi 29$ bacteriophage. The bending stiffness A corresponds to room temperature and a persistence length of 50 nm.

3.1.2 Surface energy

So far in the discussion of the inverse spool model, no consideration was made for the possibility of surface effects at the boundary of the DNA condensate. As a result, the DNA

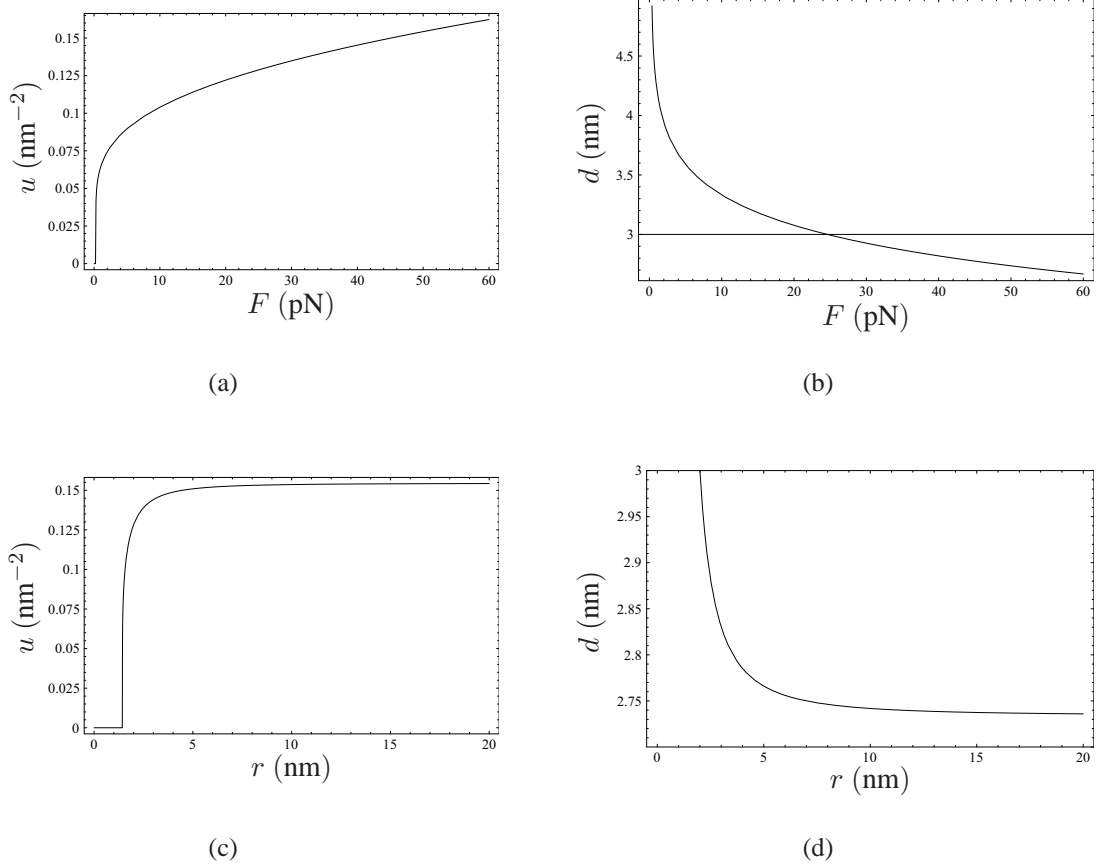


Figure 3.3: Density and spacing for $\phi 29$ with fully repulsive potential: (a) Density vs. force at the outer radius $R = 21$ nm. (b) Spacing vs. force at the outer radius $R = 21$ nm. (c) Density vs. radius at full packing. (d) Spacing vs. radius at full packing.

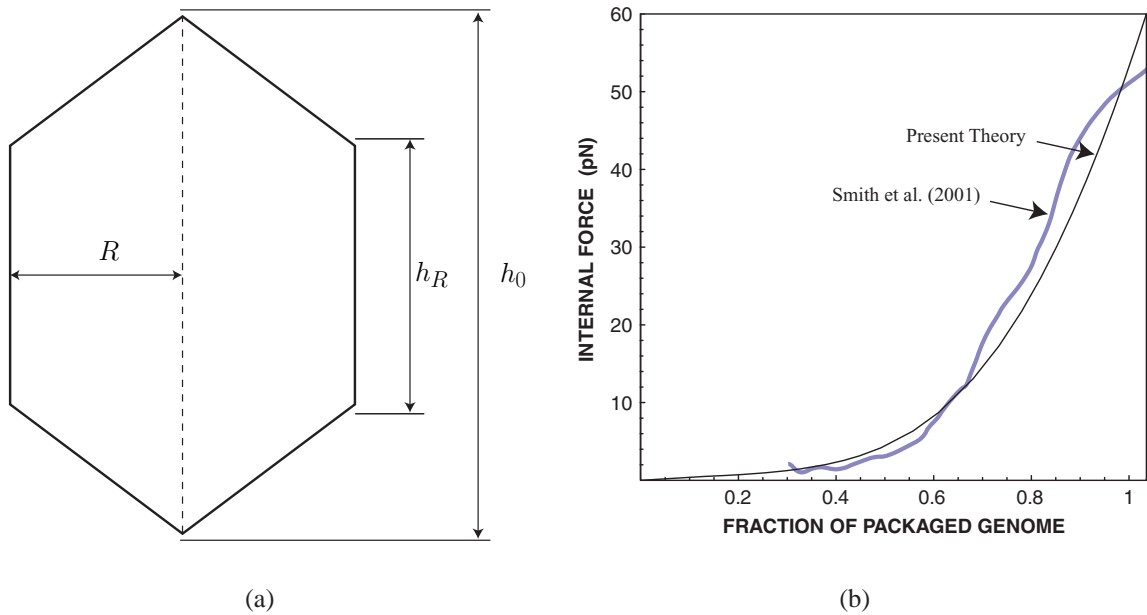


Figure 3.4: Inverse spool construction. a) Assumed geometry of ϕ 29 bacteriophage. b) Internal force vs. fraction of genome packaged.

density was shown to be only a function of the radial position r and to have no dependence on the height position z . Thus, the final shape of the condensate was governed by the geometry of the capsid and the inner-core radius at which the density vanished. Neglect of condensate surface effects is tacitly equivalent to a two-part assumption, that:

- (a) the interactions at the condensate boundary between the DNA and the capsid will be effectively the same as the DNA self interactions in the interior of the condensate, and
- (b) every point on the condensate boundary be either coincident with the capsid wall or a terminus of a decaying-to-zero density trajectory (like at the inner-core radius).

These are reasonable assumptions, especially under the tight conditions under which the genome is fully packaged. However, one interesting but so far neglected possibility is to allow for a jump in the DNA density at points on the condensate boundary which are not adjacent to the capsid wall. We examine this possibility in this section by adding a surface energy term to the total energy functional, and treating the boundary profile of the capsid (a

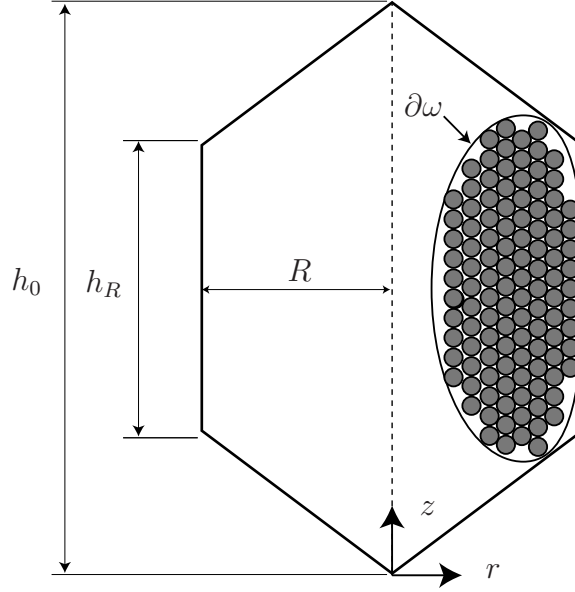


Figure 3.5: Inverse pool modeled with surface energy effects.

meridional curve in the in the r - z plane) as an unknown of the problem. As will be shown, the density then becomes a function of both r and z .

Let $\omega \subset \mathbb{R}^2$ denote the cross section (in the r - z plane) of the region occupied by DNA, as depicted in Figure 3.5. In principle ω must be treated as an unknown of the problem. That is, a profile of the condensate is sought which *minimizes* the total energy. Thus the two principal unknowns of the problem are ω which expresses the shape of the condensate, and u which specifies the density of DNA within the condensate and which, in general, may be a function of position (r, z) .

With the inclusion of surface energy, the total energy is a specialization of Equation (2.2.31) to the axisymmetric case

$$E(u, \omega) = \int_{\omega} \left\{ \frac{Au(r)}{2r^2} + \phi(u(r)) \right\} 2\pi r \, dr dz + \int_{\partial\omega} \gamma(u(r)) 2\pi r \, ds. \quad (3.1.16)$$

The length constraint $\int_{\Omega} |\mathbf{m}| dV = L$ may again be conveniently enforced by the introduction of a Lagrange multiplier F , leading to the Lagrangian

$$I(u, \omega, F) = 2\pi \int_{\omega} \left\{ \frac{Au(r)}{2r} + [\phi(u(r)) - Fu(r)]r \right\} dr dz + 2\pi \int_{\partial\omega} \gamma(u(r))r ds. \quad (3.1.17)$$

Expressions for the unknowns u and ω should be given as results of the minimization of (3.1.17). To make the problem more tractable, we assume that the boundary of the cross section is symmetric about the r -axis and can be parameterized by a single-valued function $\zeta(r)$ such that $z = \pm\zeta(r)$ on $\partial\omega$ (for a related treatment, see Ubbink and Odijk, 1996). The assumption of symmetry is suggested by the symmetry properties of the capsid models under consideration (e.g., sphere, and capped cylinder). The assumption of a single-valued parameterization $\zeta(r)$ is justifiable given the tendency of DNA condensates to adopt circular cross sections, those which minimize condensate surface area. With this parameterization of the boundary in place, the lagrangian then takes the form,

$$I(u, \zeta, F) = 4\pi \int_{R_{\text{in}}}^{R_{\text{out}}} \left(\left\{ \frac{Au}{2r} + [\phi(u) - Fu]r \right\} \zeta + \gamma(u)r\sqrt{1 + \zeta'^2} \right) dr, \quad (3.1.18)$$

where R_{in} and R_{out} are the inner and outer radii of the condensate, and $'$ indicates the derivative with respect to r .

Minimization of (3.1.18) requires that its first variation be zero. This involves variations of both u and ζ

$$\begin{aligned} 0 &= \delta I(u, \omega, F) \\ &= 4\pi \int_{R_{\text{in}}}^{R_{\text{out}}} \left(\left\{ \frac{A}{2r} + [D\phi(u) - F]r \right\} \zeta(r) + D\gamma(u)r\sqrt{1 + \zeta'^2} \right) \delta u dr \\ &\quad + 4\pi \int_{R_{\text{in}}}^{R_{\text{out}}} \left(\left\{ \frac{Au}{2r} + [\phi(u) - Fu]r \right\} \delta\zeta + \gamma(u)r \frac{\zeta' \delta\zeta'}{\sqrt{1 + \zeta'^2}} \right) dr, \end{aligned} \quad (3.1.19)$$

where D denotes the ordinary derivative. Integrating by parts to remove the derivative from $\delta\zeta$,

$$\begin{aligned} & \int_{R_{\text{in}}}^{R_{\text{out}}} \left(\left\{ \frac{A}{2r} + [D\phi(u) - F]r \right\} \zeta(r) + D\gamma(u)r\sqrt{1 + \zeta'^2} \right) \delta u \, dr \\ & + \int_{R_{\text{in}}}^{R_{\text{out}}} \left(\left\{ \frac{Au}{2r} + [\phi(u) - Fu]r \right\} - \frac{d}{dr} \left\{ \frac{\gamma(u)r\zeta'}{\sqrt{1 + \zeta'^2}} \right\} \right) \delta\zeta \, dr = 0. \end{aligned} \quad (3.1.20)$$

From this, two Euler-Lagrange equations are clearly identified,

$$\left\{ \frac{A}{2r} + [D\phi(u(r)) - F]r \right\} \zeta(r) + D\gamma(u(r))r\sqrt{1 + \zeta'^2} = 0, \quad r \in [R_{\text{in}}, R_{\text{out}}] \quad (3.1.21a)$$

$$\left\{ \frac{Au}{2r} + [\phi(u(r)) - Fu(r)]r \right\} - \frac{d}{dr} \left\{ \frac{\gamma(u(r))r\zeta'}{\sqrt{1 + \zeta'^2}} \right\} = 0, \quad r \in [R_{\text{in}}, R_{\text{out}}]. \quad (3.1.21b)$$

Equation (3.1.21) is a system of coupled nonlinear ordinary differential equations, of *first order* in $u(r)$ and *second order* in $\zeta(r)$. The necessary boundary conditions are treated shortly.

Notice that our problem is equivalent to one of Lagrangian dynamics with the role of generalized time played by r ; generalized coordinates given by $\mathbf{q} = \{u, \zeta\}$; a Lagrangian $L(\mathbf{q}, \dot{\mathbf{q}}, t)$ given by the integrand of Eqn. (3.1.18),

$$L(u, \zeta, \zeta', r) = \left\{ \frac{Au}{2r} + [\phi(u) - Fu]r \right\} \zeta + \gamma(u)r\sqrt{1 + \zeta'^2};$$

and Hamilton's Principle expressed by Eqn. (3.1.19). The second-order Lagrange's equations in (3.1.21) can be rewritten as first-order equations by computing the associated generalized momenta $\mathbf{p} = \frac{\partial L}{\partial \dot{\mathbf{q}}}$ and Hamiltonian $H(\mathbf{q}, \mathbf{p}, t) = \mathbf{p} \cdot \dot{\mathbf{q}} - L(\mathbf{q}, \dot{\mathbf{q}}, t)$, and then computing Hamilton's canonical equations

$$\dot{\mathbf{q}} = \frac{\partial H}{\partial \mathbf{p}}$$

$$\dot{\mathbf{p}} = -\frac{\partial H}{\partial \mathbf{q}}.$$

For the current problem, the Lagrangian does not depend explicitly on $\frac{du}{dr}$, so the generalized momentum conjugate to u is zero. The other generalized momentum is

$$p = \frac{\partial L}{\partial \zeta'} = \gamma(u)r \frac{\zeta'}{\sqrt{1 + \zeta'^2}}. \quad (3.1.22)$$

The Hamiltonian is

$$H(u, \zeta, p, r) = - \left\{ \frac{Au}{2r} + [\phi(u) - Fu]r \right\} \zeta - \gamma(u)r \sqrt{1 - \left(\frac{p}{\gamma(u)r} \right)^2}. \quad (3.1.23)$$

Hamilton's canonical equations, then, provide a *first-order* system which is equivalent to Eqns. (3.1.21a, b)

$$0 = \left\{ \frac{A}{2r} + [D\phi(u) - F]r \right\} \zeta + \frac{D\gamma(u) r}{\sqrt{1 - \left(\frac{p}{\gamma(u)r} \right)^2}} \quad (3.1.24a)$$

$$\zeta' = \frac{\frac{p}{\gamma(u)r}}{\sqrt{1 - \left(\frac{p}{\gamma(u)r} \right)^2}} \quad (3.1.24b)$$

$$p' = \frac{Au}{2r} + [\phi(u) - Fu]r \quad (3.1.24c)$$

As an aside, note that by neglecting the surface energy, (3.1.24a) simplifies to become equivalent to (3.1.15) as expected. When combined with the appropriate initial conditions this system can be integrated (numerically) to yield solutions for $u(r)$ and $\zeta(r)$. The boundary conditions for the system are

$$\zeta(R_{\text{out}}) = 0 \quad (3.1.25a)$$

$$\zeta'(R_{\text{out}}) = -\infty \quad (3.1.25b)$$

$$\zeta(R_{\text{in}}) = 0 \quad (3.1.25c)$$

$$\zeta'(R_{\text{in}}) = +\infty. \quad (3.1.25d)$$

However, we note that, in general, R_{out} and R_{in} are unknown. If either one is specified, then the two corresponding boundary conditions for ζ and ζ' are sufficient to integrate (3.1.24)

numerically. In this manner, a “shooting” method could be used to solve the BVP.

Instead, for the present we proceed with the simplifying assumption of the hard-core cohesive energy (2.2.20) under which $u = u_0$, if $\{r, z\} \in \omega$. This leaves $\zeta(r)$ as the only remaining unknown. Recall that

$$\begin{aligned}\phi(u_0) &= \phi_0 - \mu_0 u_0 \\ \gamma(u_0) &= \frac{-\phi(u_0)}{2\sqrt{2u_0/\sqrt{3}}} = \frac{\mu_0 u_0 - \phi_0}{2\sqrt{2u_0/\sqrt{3}}}.\end{aligned}$$

Under such an assumption, the E-L equation (3.1.21) becomes

$$\frac{Au_0}{2r} + [\phi(u_0) - Fu_0]r - \frac{d}{dr} \left\{ \frac{\gamma(u_0)r\zeta'}{\sqrt{1+\zeta'^2}} \right\} = 0, \quad r \in [R_{\text{in}}, R_{\text{out}}] \quad (3.1.26)$$

where all functions of u are now constant, such that the first integral becomes,

$$\frac{Au_0}{2} \log(r) + [\phi(u_0) - Fu_0] \frac{r^2}{2} - \frac{\gamma(u_0)r\zeta'}{\sqrt{1+\zeta'^2}} = C. \quad (3.1.27)$$

It is convenient to define an angle α such that $\zeta' \equiv -\cot \alpha$. (Physically, α is the angle that the outward normal to $\partial\omega$ makes with the r -axis.) Then $\sqrt{1+\zeta'^2} = \sqrt{1+\cot^2 \alpha} = |\csc \alpha|$, and equations (3.1.27) takes the form

$$\frac{Au_0}{2} \log r + [\phi(u_0) - Fu_0] \frac{r^2}{2} + \gamma(u_0)r \cos \alpha(r) = C. \quad (3.1.28)$$

The boundary condition $\zeta'(R_{\text{out}}) = -\infty$ becomes $\alpha(R_{\text{out}}) = 0$. Enforcing this, we get

$$Au_0 \log(r/R_{\text{out}}) + [\phi(u_0) - Fu_0](r^2 - R_{\text{out}}^2) + 2\gamma(u_0)[r \cos \alpha(r) - R_{\text{out}}] = 0. \quad (3.1.29)$$

Rearranging (3.1.29) we find an expression for $\alpha(r)$,

$$\alpha(r) = \arccos \left\{ \frac{R_{\text{out}}}{r} - \frac{Au_0 \log(r/R_{\text{out}}) + [\phi(u_0) - Fu_0](r^2 - R_{\text{out}}^2)}{2\gamma(u_0)r} \right\}. \quad (3.1.30)$$

We can now compute $\zeta(r)$ to within a constant by integrating $\zeta'(r)$,

$$\begin{aligned}\zeta(r) - \zeta(R_{\text{out}}) &= \int_{R_{\text{out}}}^r \frac{dz}{dr}(r) dr = \int_{R_{\text{out}}}^r \zeta'(r) dr \\ &= \int_{R_{\text{out}}}^r -\cot \alpha(r) dr = \int_{R_{\text{out}}}^r -\frac{\cos \alpha(r)}{\sqrt{1 - \cos^2 \alpha(r)}} dr .\end{aligned}\quad (3.1.31)$$

However, R_{out} and R_{in} are still unknown. A relationship between them can be obtained by enforcing constraint (3.1.25d), i.e., $\zeta'(R_{\text{in}}) = +\infty \Rightarrow \alpha(R_{\text{in}}) = \pi$, giving

$$Au_0 \log(R_{\text{out}}/R_{\text{in}}) + [\phi(u_0) - Fu_0](R_{\text{out}}^2 - R_{\text{in}}^2) + 2\gamma(u_0)(R_{\text{in}} + R_{\text{out}}) = 0 .\quad (3.1.32)$$

The two remaining boundary conditions (3.1.25a, b)

$$\zeta(R_{\text{out}}) = \zeta(R_{\text{in}}) = 0$$

can be combined with equation (3.1.31) to yield

$$0 = \int_{R_{\text{out}}}^{R_{\text{in}}} -\frac{\cos \alpha(r)}{\sqrt{1 - \cos^2 \alpha(r)}} dr\quad (3.1.33)$$

which can be solved simultaneously with (3.1.32) to produce values for R_{in} and R_{out} .

Figure 3.6 shows resulting boundary profiles for $z = +\zeta(r)$ for several packing percentages in the $\phi 29$ capsid. The dimensions of the capsid are shown in Table 3.2. The value of ϕ_0 is borrowed directly from Kindt et al. (2001). The value of μ_0 was adjusted such that a toroidal condensate would be formed having known dimensions (Arscott et al., 1990). The predictions of the present theory show that at low packing ratio the condensate has a circular meridional profile, reminiscent of toroidal condensates found in solution (Arscott et al., 1990). With increasing packing ratio, the outer edge of the condensate moves toward contact with the capsid wall where it is eventually constrained. The profile near the inner edge of the condensate flattens, eventually taking a spool-like shape. We note that these results are consistent with the predictions of Kindt et al. (2001) showing a gradual evolution in shape from a torus-shaped condensate to the inverse spool.

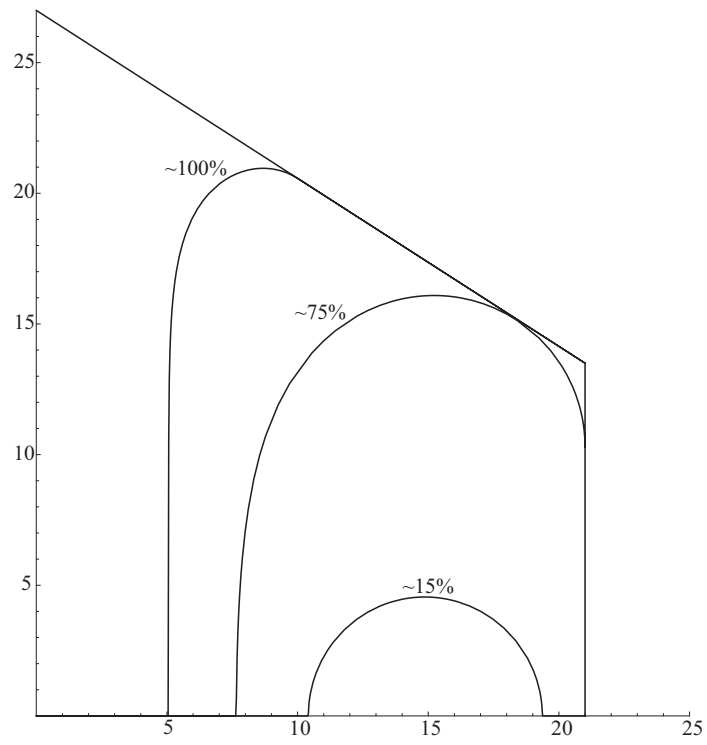


Figure 3.6: Surface contours of DNA at different forces within the $\phi 29$ capsid. (Axes measure position in nm.)

R (nm)	h_0 (nm)	h_R (nm)	A (pN \times nm ²)	ϕ_0 (pN nm ⁻²)	μ_0 (pN)	u_0 nm ⁻²
21.00	54.00	27.00	202.31	0.4937	7.026	0.1473

Table 3.2: Assumed constants for ϕ 29 bacteriophage. Hard-core, constant-density cohesive energy model.

3.2 Torsionless toroidal solenoids

In the remainder of the chapter we endeavor to find competing constructions which improve upon the baseline inverse spool DNA conformation just described. The inverse spool conformation may be expected to become too costly near the axis of the capsid, where the curvature of the coils in the spool becomes large. In that region, it is energetically advantageous to arrange the DNA *parallel* to the axis of the capsid. Since the DNA strand must be continuous, the core axial DNA must close and form loops. This suggests considering DNA arrangements in the form of *solenoids*, i.e., helical coils wrapped around toroids centered on the capsid axis. In this section, we analyze the case of *torsionless toroidal solenoids*, consisting of planar coils contained within meridional planes, Figure 3.7. For simplicity, we restrict attention to problem (2.2.28), i.e., we concern ourselves with the problem of finding the energy-minimizing conformations of the entire genome within the capsid.

With reference to the cylindrical coordinate system introduced in the preceding section, we now consider solutions of the form

$$t_r = t_r(r, z), \quad t_\theta = 0, \quad t_z = t_z(r, z). \quad (3.2.1)$$

Conformations of this type consist of planar—and hence torsionless—DNA coils lying on meridional or r - z planes.² Each closed coil defines the cross section of a toroid centered on the z axis. The DNA coils wrap around those toroids, and hence we shall refer to this type of DNA arrangement as a *torsionless toroidal solenoid*. For this geometry, the divergence constraint becomes

$$\nabla \cdot \mathbf{t} = \frac{1}{r} \frac{\partial}{\partial r}(rt_r) + \frac{\partial t_z}{\partial z} = 0, \quad (3.2.2)$$

²Again, as was true for the inverse spool, the pitch (and thus, the t_θ component) would not be strictly zero for an actual, one-dimensional-continuum DNA strand, but for the level of resolution of this model, any slight pitch can be safely neglected.

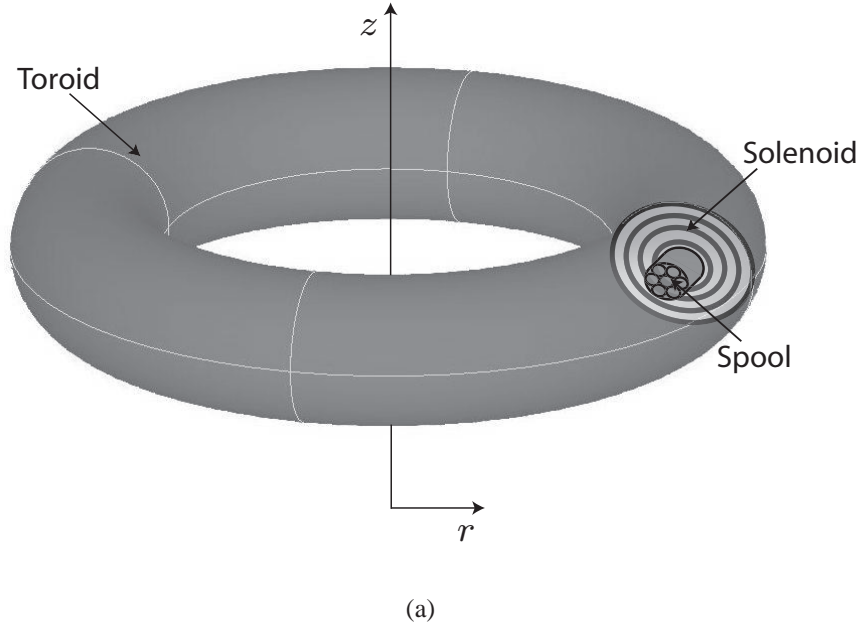


Figure 3.7: Geometry of torsionless toroidal solenoid.

and the modulus constraint takes the form

$$|\mathbf{t}|^2 = t_r^2 + t_z^2 = 1. \quad (3.2.3)$$

In addition, the curvature (2.1.10a) reduces to

$$\kappa^2 = |\mathbf{t} \cdot \nabla \mathbf{t}|^2 = \left(t_r \frac{\partial t_r}{\partial r} + t_z \frac{\partial t_r}{\partial z} \right)^2 + \left(t_r \frac{\partial t_z}{\partial r} + t_z \frac{\partial t_z}{\partial z} \right)^2. \quad (3.2.4)$$

This expression can be further simplified with the aid of the modulus constraint (3.2.3), which requires that $\mathbf{t} = \{\cos \varphi, 0, \sin \varphi\}$. Inserting this representation into (3.2.4) gives, after some trite calculations,

$$\kappa^2 = \left(\cos \varphi \frac{\partial \varphi}{\partial r} + \sin \varphi \frac{\partial \varphi}{\partial z} \right)^2 = \varphi'^2, \quad (3.2.5)$$

which is the known result for planar rods, namely, that the curvature is the derivative of the polar angle of the tangent with respect to the arc-length. Expression (3.2.5) can be

re-written in the form

$$\kappa^2 = \left(\frac{\partial t_z}{\partial r} - \frac{\partial t_r}{\partial z} \right)^2. \quad (3.2.6)$$

In the regions where the DNA is arranged in the geometry (3.2.1) the strain energy density reduces to the form

$$W(\mathbf{t}, \nabla \mathbf{t}) = \frac{Au_0}{2} \kappa^2 = \frac{Au_0}{2} \left(\frac{\partial t_z}{\partial r} - \frac{\partial t_r}{\partial z} \right)^2. \quad (3.2.7)$$

Consider now a torsionless toroidal solenoid of known smooth boundary $\partial\omega$. We wish to determine the structure of the DNA contained within the coil. To this end, we begin by noting that the divergence constraint (3.2.2) may be identically satisfied by the introduction of a vector potential, $\mathbf{v} = \{0, v_\theta(r, z), 0\}$, such that

$$t_r = -\frac{\partial v_\theta}{\partial z}, \quad t_z = \frac{1}{r} \frac{\partial}{\partial r}(rv_\theta) = \frac{v_\theta}{r} + \frac{\partial v_\theta}{\partial r}, \quad (3.2.8)$$

whereupon the modulus constraint (3.2.3) becomes

$$\left(\frac{1}{r} \frac{\partial}{\partial r}(rv_\theta) \right)^2 + \left(\frac{\partial v_\theta}{\partial z} \right)^2 = 1. \quad (3.2.9)$$

Finally, the tangency boundary condition on $\partial\omega$ may be enforced by appending the boundary condition

$$v_\theta = 0, \quad \text{on } \partial\omega. \quad (3.2.10)$$

Indeed, since by this choice of boundary condition $\partial\omega$ is a level contour of v_θ , it follows that $\boldsymbol{\nu} \propto \{\partial v_\theta/\partial r, 0, \partial v_\theta/\partial z\}$, and Eqs. (3.2.8) give $\mathbf{t} \cdot \boldsymbol{\nu} = 0$, as required.

Multiplication of (3.2.9) by $r^2/2$ gives

$$F(\mathbf{p}, \eta, r) \equiv \frac{1}{2}(p_r^2 + p_z^2) - \frac{1}{2}r^2 = 0, \quad (3.2.11)$$

where

$$\eta = rv_\theta, \quad p_r = \frac{\partial \eta}{\partial r}, \quad p_z = \frac{\partial \eta}{\partial z}. \quad (3.2.12)$$

We note that in terms of η Eqs. (3.2.8) become

$$t_r = -\frac{1}{r} \frac{\partial \eta}{\partial z}, \quad t_z = \frac{1}{r} \frac{\partial \eta}{\partial r}, \quad (3.2.13)$$

which shows that \mathbf{t} is tangent to the level contours of η , i.e.,

$$t_r \frac{\partial \eta}{\partial r} + t_z \frac{\partial \eta}{\partial z} = 0. \quad (3.2.14)$$

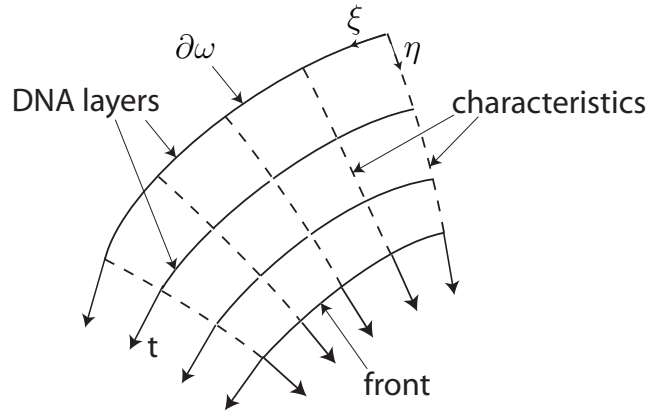


Figure 3.8: Schematic of characteristic construction for the solenoid DNA conformation.

The first-order partial-differential equation (3.2.11) is an inhomogeneous variant of the *eikonal* equation which can be solved by the method of characteristics. The characteristic equations for the first-order PDE (3.2.11) are (e.g., Evans, 1998)

$$\dot{r} = \frac{\partial F}{\partial p_r} = p_r \quad (3.2.15a)$$

$$\dot{z} = \frac{\partial F}{\partial p_z} = p_z \quad (3.2.15b)$$

$$\dot{p}_r = -\frac{\partial F}{\partial r} - \frac{\partial F}{\partial \eta} p_r = r \quad (3.2.15c)$$

$$\dot{p}_z = -\frac{\partial F}{\partial z} - \frac{\partial F}{\partial \eta} p_z = 0 \quad (3.2.15d)$$

$$\dot{\eta} = \frac{\partial F}{\partial p_r} p_r + \frac{\partial F}{\partial p_z} p_z = p_r^2 + p_z^2. \quad (3.2.15e)$$

In addition, appropriate boundary conditions must be supplied. To this end, let the boundary $\partial\omega$ be defined parametrically as

$$r = r_0(\xi), \quad z = z_0(\xi), \quad (3.2.16)$$

where ξ denotes the arc-length measured along $\partial\omega$. From the tangency condition ($\mathbf{t} \cdot \boldsymbol{\nu} = 0$ on $\partial\Omega$), it follows that η must be constant, e.g., zero, on $\partial\omega$. Thus, the complete set of boundary conditions for the characteristic problem is (Evans, 1998)

$$\eta(\xi, 0) = 0 \quad (3.2.17a)$$

$$p_r(\xi, 0)r'_0(\xi) + p_z(\xi, 0)z'_0(\xi) = 0 \quad (3.2.17b)$$

$$\frac{1}{2}(p_r^2(\xi, 0) + p_z^2(\xi, 0)) - \frac{1}{2}r_0^2(\xi) = 0. \quad (3.2.17c)$$

The characteristic problem just posed can be solved analytically as follows. Begin by combining (3.2.15a)–(3.2.15d) to obtain

$$\ddot{r} - r = 0, \quad \ddot{z} = 0. \quad (3.2.18)$$

A first integral of the problem can now be obtained by multiplying the first of this by \dot{r} and the second by \dot{z} and adding the resulting equations to form a perfect differential, which upon integration gives

$$\frac{1}{2}(\dot{r}^2 + \dot{z}^2) - \frac{1}{2}r^2 = C. \quad (3.2.19)$$

But the boundary condition (3.2.17c) requires that $C = 0$, and thus we have

$$\dot{\eta} = \dot{r}^2 + \dot{z}^2 = r^2, \quad (3.2.20)$$

where we have made additional use of Eqs. (3.2.15a), (3.2.15b) and (3.2.15e). Next we note that, if the parametric equations of an arbitrary level contour $\eta = \eta_0 \geq 0$ are known, the characteristic problem can be restarted from this contour. Then, the compatibility condition (3.2.17b) in conjunction with the orthogonality property (3.2.14) imply generally that \mathbf{t} is

orthogonal to \mathbf{p} , which in view of (3.2.15a) and (3.2.15b) in turn requires

$$\dot{r} = -\lambda t_z = -\lambda \sin \varphi, \quad \dot{z} = \lambda t_r = \lambda \cos \varphi \quad (3.2.21)$$

for some scalar λ . Inserting this representation into the first integral (3.2.20) identifies λ as r , and we have

$$\dot{r} = -r \sin \varphi, \quad \dot{z} = r \cos \varphi. \quad (3.2.22)$$

Differentiating (3.2.22) and using (3.2.15a,b) and (3.2.22) again to eliminate either \dot{r} and \ddot{r} , or \dot{z} and \ddot{z} gives, after some simplification,

$$\dot{\varphi} = -\cos \varphi. \quad (3.2.23)$$

The solution of (3.2.18) is elementary and takes the form

$$r(\xi, t) = r_0(\xi) \cosh t - r_0(\xi) z'_0(\xi) \sinh t, \quad (3.2.24a)$$

$$z(\xi, t) = z_0(\xi) + r_0(\xi) r'_0(\xi) t, \quad (3.2.24b)$$

where we have used (3.2.22) to derive the identities $\dot{r}(0) = -r_0 \sin \varphi_0 = -r_0 z'_0$ and $\dot{z}(0) = r_0 \cos \varphi_0 = r_0 r'_0$. Inserting (3.2.24a) into (3.2.20) and integrating with respect to t further gives

$$\eta(\xi, t) = \frac{1}{2} r_0'^2(\xi) r_0^2(\xi) t + \frac{1}{2} z_0'(\xi) r_0^2(\xi) (1 - \cosh(2t)) + \frac{1}{4} (1 + z_0'^2(\xi)) r_0^2(\xi) \sinh(2t). \quad (3.2.25)$$

Finally, from (3.2.18) and (3.2.22) we obtain the identity

$$\dot{z} = \dot{z}_0 = r_0(\xi) r'_0(\xi) = r \cos \varphi, \quad (3.2.26)$$

which can be solved for φ , with the result

$$\varphi(\xi, t) = \arccos \left(\frac{r_0(\xi) r'_0(\xi)}{r(\xi, t)} \right), \quad (3.2.27)$$

where $r(\xi, t)$ is given by (3.2.24a).

The parameter t can be eliminated from (3.2.25) in favor of η , resulting in relations of the form

$$r = r(\xi, \eta), \quad z = z(\xi, \eta), \quad \varphi = \varphi(\xi, \eta), \quad (3.2.28)$$

which are fully determined once the boundary $\partial\omega$ is specified. The first two Eqs. of (3.2.28) may be regarded as defining a system of curvilinear coordinates (ξ, η) , Figure 3.8. The system is orthogonal by virtue of the orthogonality property (3.2.14). The coordinate lines $\xi = \text{constant}$ coincide with the characteristic trajectories, whereas the lines $\eta = \text{constant}$ trace the DNA strand. The metric tensor corresponding to the (ξ, η) coordinates is diagonal, and the diagonal components are

$$h_\xi^2 = \left(\frac{\partial r}{\partial \xi}\right)^2 + \left(\frac{\partial z}{\partial \xi}\right)^2, \quad h_\eta^2 = \left(\frac{\partial r}{\partial \eta}\right)^2 + \left(\frac{\partial z}{\partial \eta}\right)^2, \quad (3.2.29)$$

which can be computed from (3.2.28).

In order to evaluate the bending energy of the DNA in the coil, we recall that the curvature follows from relation (3.2.5), which in characteristic coordinates becomes

$$\kappa^2 = \frac{1}{h_\xi^2} \left(\frac{\partial \varphi}{\partial \xi}\right)^2, \quad (3.2.30)$$

and the bending energy of the DNA in the region $0 \leq \eta \leq N$ follows as

$$E(\partial\omega, N) = \int_0^N \frac{A}{2} \kappa^2 h_\xi h_\eta d\xi d\eta = \int_0^N \frac{A}{2} \left(\frac{\partial \varphi}{\partial \xi}\right)^2 \frac{h_\eta}{h_\xi} d\xi d\eta. \quad (3.2.31)$$

As the DNA front propagates into the interior of the solenoid, the curvature increases and, beyond some value N of η , the spool conformation becomes preferable. Specifically, it is energetically advantageous to add a new layer to the solenoid if the bending energy of such layer is less than the bending energy of the corresponding volume of DNA in the spool conformation, i.e., if

$$\int_{\eta=\text{const}} \frac{A}{2} \kappa^2 h_\xi h_\eta d\xi \leq \int_{\eta=\text{const}} \frac{A}{2} \frac{1}{r^2} h_\xi h_\eta d\xi. \quad (3.2.32)$$

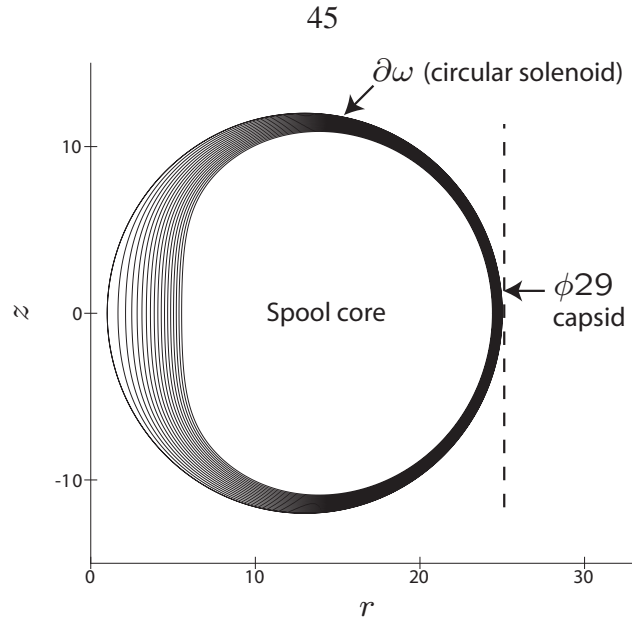


Figure 3.9: Torsionless toroidal solenoid of circular cross section.

Therefore, the solenoid terminates at a depth N such that

$$\int_{\eta=N} \frac{A}{2} \kappa^2 h_\xi h_\eta d\xi = \int_{\eta=N} \frac{A}{2} \frac{1}{r^2} h_\xi h_\eta d\xi, \quad (3.2.33)$$

and the remaining core of the domain ω is occupied by DNA in the spool conformation. It therefore follows that the DNA structure within a torsionless toroidal solenoid is fully determined by the divergence and modulus constraints once the outer contour $\partial\omega$ of the solenoid is known.

It is readily verified that solenoids can indeed beat inverse spools at the game of energy minimization. For instance, consider a solenoid of circular cross section centered at $r = 13$ nm, and of radius of 12 nm. The corresponding DNA structure is shown in Figure 3.9. It is interesting to note from this figure the combined effect of the divergence constraint and the distance to the axis, which requires the coils to be more widely spaced near the axis. Using the parameters collected in Table 3.1, the energy difference between the solenoid and spool conformations is computed to be $\Delta E \approx -1.45 \times 10^3$ pN \times nm, which shows that the solenoid does indeed beat the spool conformation. In order to gage the magnitude of this energy differential, we may recall that the work required to package the entire genome

of the $\phi 29$ bacteriophage has been experimentally estimated by Smith et al. (2001) to be of the order of 7.5×10^4 pN \times nm. It is thus concluded that the energy advantage afforded by the solenoid structure is non-negligible on that scale, which in turn suggests that motifs other than the inverse spool are likely to also occur in nature.

We close this section by noting that the characteristic construction which determines the coil geometry within torsionless toroidal solenoids is, in essence, a geometrical optics construction in which the wave fronts trace the DNA strand. In such cases, Fermat's principle provides an alternative characterization of the solution. To this end, introduce the *optical* distance between two points \mathbf{x}_1 and \mathbf{x}_2 in ω as

$$d(\mathbf{x}_1, \mathbf{x}_2) = \inf_{\gamma} \oint_{\gamma} r ds, \quad (3.2.34)$$

where the infimum is taken over all piecewise differentiable paths γ of class C^1 joining \mathbf{x}_1 and \mathbf{x}_2 , and s measures the arc-length on γ . For any point $\mathbf{x} \in \omega$, the escape distance from \mathbf{x} to $\partial\omega$ is now defined as

$$\eta(\mathbf{x}) = \inf_{\xi} d(\mathbf{x}, \mathbf{x}(\xi)), \quad (3.2.35)$$

and Fermat's principle states that this escape distance is indeed a solution of the characteristic problem. Evidently, the paths which give the optical distance (3.2.34) are geodesics in the (r, z) plane corresponding to the metric $ds^2 = r^2 dr^2 + r^2 dz^2$, and coincide with the solutions of the characteristic Eqs. (3.2.18).

3.3 Solenoid/spool mixtures

The torsionless toroidal solenoids introduced in the preceding section may be regarded as *two-phase* DNA structures, the constituent phases being the solenoid and spool arrangements. Examples, such as the circular toroid discussed in the foregoing, show that combinations of the two phases are generally preferable to single-phase arrangements. Suppose that, at every point within the capsid, the DNA can choose freely between the solenoid and

spool phases. The strain energy density of the DNA is then of the *two-well* form

$$W(r, \mathbf{t}) = \frac{Au_0}{2} \left\{ \left(\frac{\partial t_z}{\partial r} - \frac{\partial t_r}{\partial z} \right)^2 \wedge \frac{1}{r^2} \right\}, \quad (3.3.1)$$

where $a \wedge b = \min\{a, b\}$. The central question is then which is the optimal, or energy-minimizing, two-phase DNA structure. We note that, owing to the divergence constraint, the choice of phase cannot be decided in a purely local fashion. In particular, DNA loops must close properly, which places nonlocal topological constraints on the spatial phase distribution.

3.3.1 Equilibrium solenoid/spool interfaces

We begin by considering the related question of the configurational equilibrium of solenoid/spool interfaces. As in any phase mixture, to each solenoid/spool interface we can associate a *configurational force*. These configurational forces are energetic forces conjugate to normal displacements of the interface and, hence, they vanish for an energy-minimizing phase distribution. Specifically, configurational equilibrium demands

$$f = \llbracket P_{ij} \rrbracket \nu_i \nu_j = 0, \quad (3.3.2)$$

where \mathbf{P} is the energy-momentum tensor derived in Appendix A and f is the configurational force acting on the interface. This condition may be modified in order to account for interfacial energy, but this extension will not be pursued here. In order to evaluate the form of f for solenoid/spool interfaces, we note that the divergence constraint (2.1.4) requires that

$$\mathbf{t} \cdot \boldsymbol{\nu} = 0 \quad (3.3.3)$$

at the interface. In addition, equilibrium across the interface demands

$$-Au_0 \left(\frac{\partial t_z}{\partial r} - \frac{\partial t_r}{\partial z} \right) \nu_z - \lambda \nu_r = 0, \quad (3.3.4a)$$

$$Au_0 \left(\frac{\partial t_z}{\partial r} - \frac{\partial t_r}{\partial z} \right) \nu_r - \lambda \nu_z = 0, \quad (3.3.4b)$$

which follow directly from (3.2.7) and the divergence constraint. Specializing \mathbf{P} for the energy (3.3.1) and making use of the boundary conditions (3.3.4a) and (3.3.4b), we obtain the particularly simple expression

$$f = \llbracket W \rrbracket = \frac{Au_0}{2} \left(\frac{1}{r^2} - \kappa^2 \right), \quad (3.3.5)$$

and the stationarity condition (3.3.2) becomes

$$\kappa^2 = \frac{1}{r^2}. \quad (3.3.6)$$

This equation determines the possible shapes of solenoid/spool interfaces in configurational equilibrium.

In terms of the polar angle φ of the tangent to the interface, Eq. (3.3.6) takes the form

$$\left(\frac{\partial \varphi}{\partial \xi} \right)^2 = \frac{1}{r^2}, \quad (3.3.7)$$

or, equivalently,

$$\frac{\partial \varphi}{\partial \xi} = \pm \frac{1}{r}, \quad (3.3.8)$$

Eq. (3.3.8), in conjunction with the relations

$$\frac{\partial r}{\partial \xi} = \cos \varphi, \quad \frac{\partial z}{\partial \xi} = \sin \varphi, \quad (3.3.9)$$

determines the parametric equations of the boundary $(r(\xi), z(\xi))$.

Evidently, the equilibrium interfaces are comprised of a sequence of arcs whose curvatures have alternating signs, corresponding to the two branches of (3.3.8). It suffices to

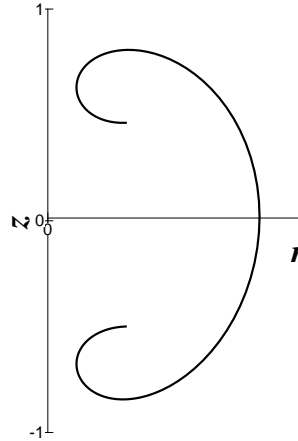


Figure 3.10: Equilibrium spool/solenoid interface.

consider the case $\kappa = 1/r$, since the remaining branch corresponds to reversing the direction of traversal of the interface. Then, a change of variables from ξ to φ reduces the remaining equations (3.3.9) to the form

$$\frac{\partial r}{\partial \varphi} = r \cos \varphi, \quad \frac{\partial z}{\partial \varphi} = r \sin \varphi. \quad (3.3.10)$$

These equations can be integrated to give

$$r(\varphi) = r_0 \exp(\sin \varphi - \sin \varphi_0), \quad (3.3.11a)$$

$$z(\varphi) = z_0 + r_0 \int_{\varphi_0}^{\varphi} \exp(\sin \psi - \sin \varphi_0) \sin \psi d\psi, \quad (3.3.11b)$$

where $r_0 = r(\varphi_0)$ and $z_0 = z(\varphi_0)$. The equilibrium interface corresponding to $r_0 = 1$, $z_0 = 0$ and $-\pi \leq \varphi \leq 3\pi$ is shown in Figure 3.10. The interface is periodic in the z direction and resembles a *prolate cycloid* in the $(\log r, z)$ plane.

3.3.2 Fine solenoid/spool mixtures

Next we consider the possibility of fine mixtures of the solenoid and spool phases. In order to describe these mixtures, we introduce an additional scalar field χ such that $\chi(\mathbf{x}) \in [0, 1]$ is the volume fraction of the solenoid phase at \mathbf{x} . Correspondingly, the complement $1 - \chi(\mathbf{x})$ is the volume fraction of the spool phase at \mathbf{x} . Consider, in particular, a closed surface S contained within the capsid. Then, conservation of mass requires that

$$\int_S (\chi \mathbf{t} u_0) \cdot \boldsymbol{\nu} dS = 0. \quad (3.3.12)$$

At points where \mathbf{t} is differentiable this places the constraint

$$\nabla \cdot (\chi \mathbf{t}) = 0, \quad (3.3.13)$$

whereas at a discontinuity surface we must have

$$[[\chi \mathbf{t}]] \cdot \boldsymbol{\nu} = 0, \quad (3.3.14)$$

generalizing (2.1.3) and (2.1.4) to mixtures. The strain energy of the DNA is now

$$W(r, \mathbf{t}, \chi) = \frac{Au_0}{2} \left\{ \chi \left(\frac{\partial t_z}{\partial r} - \frac{\partial t_r}{\partial z} \right)^2 + (1 - \chi) \frac{1}{r^2} \right\}, \quad (3.3.15)$$

and the total strain energy of the spool/coil mixture is

$$E(\mathbf{t}, \chi) = \int_\omega \frac{Au_0}{2} \left\{ \chi \left(\frac{\partial t_z}{\partial r} - \frac{\partial t_r}{\partial z} \right)^2 + (1 - \chi) \frac{1}{r^2} \right\} 2\pi r dr dz. \quad (3.3.16)$$

The problem is now to minimize the energy with respect to the fields (\mathbf{t}, χ) .

Begin by supposing that the volume-fraction field χ is known over a region ω of the (r, z) -plane, and that $\chi > 0$ in that region. Suppose, in addition, that

$$\mathbf{t} \cdot \boldsymbol{\nu} = 0, \quad \text{on } \partial\omega. \quad (3.3.17)$$

Then, as in the case of a pure solenoid, the structure of the solenoid phase within ω follows by an application of the method of characteristics. Introduce a vector potential, $\mathbf{v} = \{0, v_\theta(r, z), 0\}$, such that

$$\chi t_r = -\frac{\partial v_\theta}{\partial z}, \quad \chi t_z = \frac{1}{r} \frac{\partial}{\partial r}(r v_\theta) = \frac{v_\theta}{r} + \frac{\partial v_\theta}{\partial r}, \quad (3.3.18)$$

whereupon the modulus constraint becomes

$$\left(\frac{1}{r} \frac{\partial}{\partial r}(r v_\theta)\right)^2 + \left(\frac{\partial v_\theta}{\partial z}\right)^2 = \chi^2. \quad (3.3.19)$$

The tangency constraint (3.3.17) may be enforced by appending the boundary condition (3.2.10). Multiplication of (3.3.19) by $r^2/2$ gives

$$F(\mathbf{p}, \eta, \mathbf{x}) \equiv \frac{1}{2}(p_r^2 + p_z^2) - \frac{1}{2}\chi^2(r, z)r^2 = 0, \quad (3.3.20)$$

where η and \mathbf{p} are as in (3.2.12). As in the case of immiscible phases, we have

$$\chi t_r = -\frac{1}{r} \frac{\partial \eta}{\partial z}, \quad \chi t_z = \frac{1}{r} \frac{\partial \eta}{\partial r}, \quad (3.3.21)$$

which shows that \mathbf{t} is tangent to the level contours of η . The inhomogeneous *eikonal* equation (3.3.20) can again be solved by the method of characteristics. The characteristic equations are

$$\dot{r} = \frac{\partial F}{\partial p_r} = p_r \quad (3.3.22a)$$

$$\dot{z} = \frac{\partial F}{\partial p_z} = p_z \quad (3.3.22b)$$

$$\dot{p}_r = -\frac{\partial F}{\partial r} - \frac{\partial F}{\partial \eta} p_r = \frac{1}{2} \frac{\partial}{\partial r}(\chi^2(r, z)r^2) \quad (3.3.22c)$$

$$\dot{p}_z = -\frac{\partial F}{\partial z} - \frac{\partial F}{\partial \eta} p_z = \frac{1}{2} \frac{\partial}{\partial z}(\chi^2(r, z)r^2) \quad (3.3.22d)$$

$$\dot{\eta} = \frac{\partial F}{\partial p_r} p_r + \frac{\partial F}{\partial p_z} p_z = p_r^2 + p_z^2. \quad (3.3.22e)$$

Representing $\partial\omega$ as in (3.2.16), a complete set of boundary conditions is now

$$\eta(\xi, 0) = 0 \quad (3.3.23a)$$

$$p_r(\xi, 0)r'_0(\xi) + p_z(\xi, 0)z'_0(\xi) = 0 \quad (3.3.23b)$$

$$\frac{1}{2}(p_r^2(\xi, 0) + p_z^2(\xi, 0)) - \frac{1}{2}\chi^2(r_0(\xi), z_0(\xi))r_0^2(\xi) = 0. \quad (3.3.23c)$$

A first integral of the problem can now be obtained by multiplying (3.3.22c) by \dot{r} and (3.3.22d) by \dot{z} and adding the resulting equations to form a perfect differential, which upon integration gives

$$\frac{1}{2}(\dot{r}^2 + \dot{z}^2) - \frac{1}{2}\chi^2 r^2 = C. \quad (3.3.24)$$

But the boundary condition (3.3.23c) requires that $C = 0$, and thus we have

$$\dot{\eta} = \dot{r}^2 + \dot{z}^2 = \chi^2 r^2, \quad (3.3.25)$$

where we have made additional use of Eqs. (3.3.22a), (3.3.22b) and (3.3.22e). Proceeding as in the derivation of (3.2.22) and (3.2.23) we additionally have

$$\dot{r} = -\chi r \sin \varphi, \quad \dot{z} = \chi r \cos \varphi, \quad \dot{\varphi} = -(\chi r)'. \quad (3.3.26)$$

The preceding analysis shows that the geometry of the solenoid phase is fully determined once the domain ω and the coil volume fraction χ are specified.

Next we turn to the problem of determining χ . Let γ denote the wave front corresponding to η , and let s be the arc-length measured on γ . Consider in addition the neighboring wave front corresponding to $\eta + \Delta\eta$. From the first integral (3.3.25) it follows that the normal distance between the two neighboring wave fronts is

$$\Delta n(s) = \frac{\Delta\eta}{\chi(s)r(s)}. \quad (3.3.27)$$

Hence, to first order the energy increment attendant to the front advance is

$$\Delta E = \int_{\gamma} \frac{Au_0}{2} \left\{ \chi(s) \kappa^2(s) + (1 - \chi(s)) \frac{1}{r^2(s)} \right\} 2\pi r(s) \Delta n(s) ds. \quad (3.3.28)$$

Clearly, the energy increment per unit advance is minimized by setting $\chi(s) = 1$ over the subset $\gamma_1 \subset \gamma$ where $\kappa(s) < r^{-1}(s)$, where we take positive curvature to mean that the front is concave inward; and $\chi(s) = 0$ over the subset $\gamma_0 \subset \gamma$ where $\kappa(s) > r^{-1}(s)$. Over γ_1 , (3.3.27) gives $\Delta n(s) = \Delta\eta/r(s)$, which corresponds to the addition of a pure solenoidal layer. Over γ_0 , (3.3.27) gives $\Delta n(s) = \infty$ and the characteristic construction ceases to apply in that region. Physically, the divergence of Δn corresponds to the opening of a spool-phase gap in the solenoid.

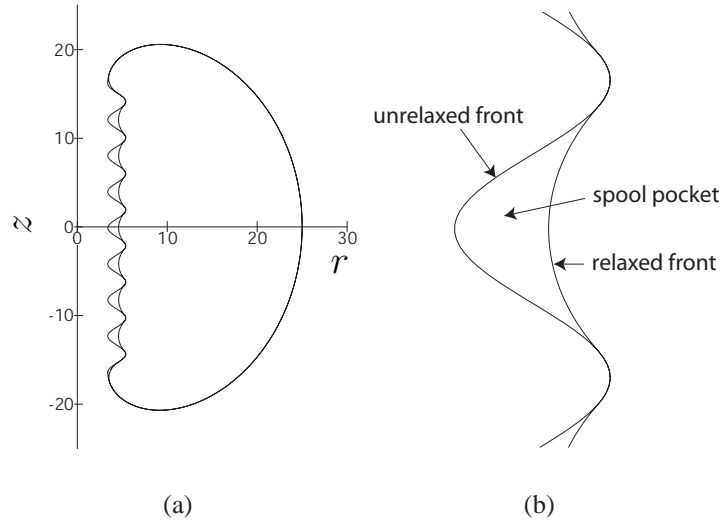


Figure 3.11: a) Relaxation of concave segments of an initial front to equilibrium interface segments. b) Closeup of the initial and relaxed fronts and the resulting spool gap.

The picture which emerges from the preceding analysis is that, in the mixed region, the DNA arrangement consists of *solenoid layers*, corresponding to $\chi = 1$, separated by *spool gaps*, corresponding to $\chi = 0$. The precise sequence of events leading to this structure is as follows. Consider a solenoid front γ . The region γ_1 of the front where $\kappa < r^{-1}$ is stable against insertion of spool pockets and propagates in accordance with the characteristic construction for $\chi = 1$, leaving behind a layer of pure solenoid phase. Contrariwise, the

region γ_0 of the front where $\kappa > r^{-1}$ is unstable and *detaches* from the solenoid, with the result that a spool gap opens up. This situation is likely to arise, e.g., over parts of the front which are about to form a caustic. Configuration equilibrium then demands that the leading edge of the newly formed spool gap be an equilibrium solenoid/spool interface. We say then that the front *relaxes* toward an equilibrium interface, or simply relaxes. That leading spool-gap edge, and the remainder γ_1 of the solenoid front, jointly define a new front, and the process repeats itself until a spool core is reached and the construction terminates.

An example of relaxation is shown in Figure 3.11. The initial solenoid front is wavy and has unstable concave regions where $\kappa > r^{-1}$, Figure 3.11a. Relaxation of the front replaces those concave regions by osculating equilibrium interfaces, Figure 3.11a and b. In principle, the relaxation could be effected by *fitting* curves of the form (3.3.11a) and (3.3.11b) against the unstable front wherever possible. This operation is highly non-local and cumbersome to implement for general front geometries. In calculations it is more convenient to relax the front iteratively by the repeated application of local operations. A simple relaxation algorithm is given in Appendix B. The relaxed front shown in Figure 3.11 is obtained using this algorithm.

3.3.3 Application to the $\phi 29$ bacteriophage

As an example of application of the construction just described, we consider a $\phi 29$ capsid idealized as a capped cylinder. The dimensions of the capsid and the remaining parameters describing the DNA are as listed in Table 1. The front is discretized into 1024 segments, and the nodes are advanced according to the exact characteristic solution (3.2.24a), (3.2.24b) and (3.2.25) at increments $\Delta\eta = 2.88 \times 10^{-3} \text{ nm}^2$, followed by an application of the relaxation iteration described in Appendix B.

The initial front is taken to coincide with the boundary of the capsid, Figure 3.12a. Since the initial front contains sharp corners, it immediately relaxes to a smooth front which contains segments of equilibrium solenoid/spool interface at the apices and shoulders of the capsid. The relaxation of the initial front leaves pockets of spool phase also at the apices and shoulders of the capsid. The subsequent propagation of the front occurs in two modes:

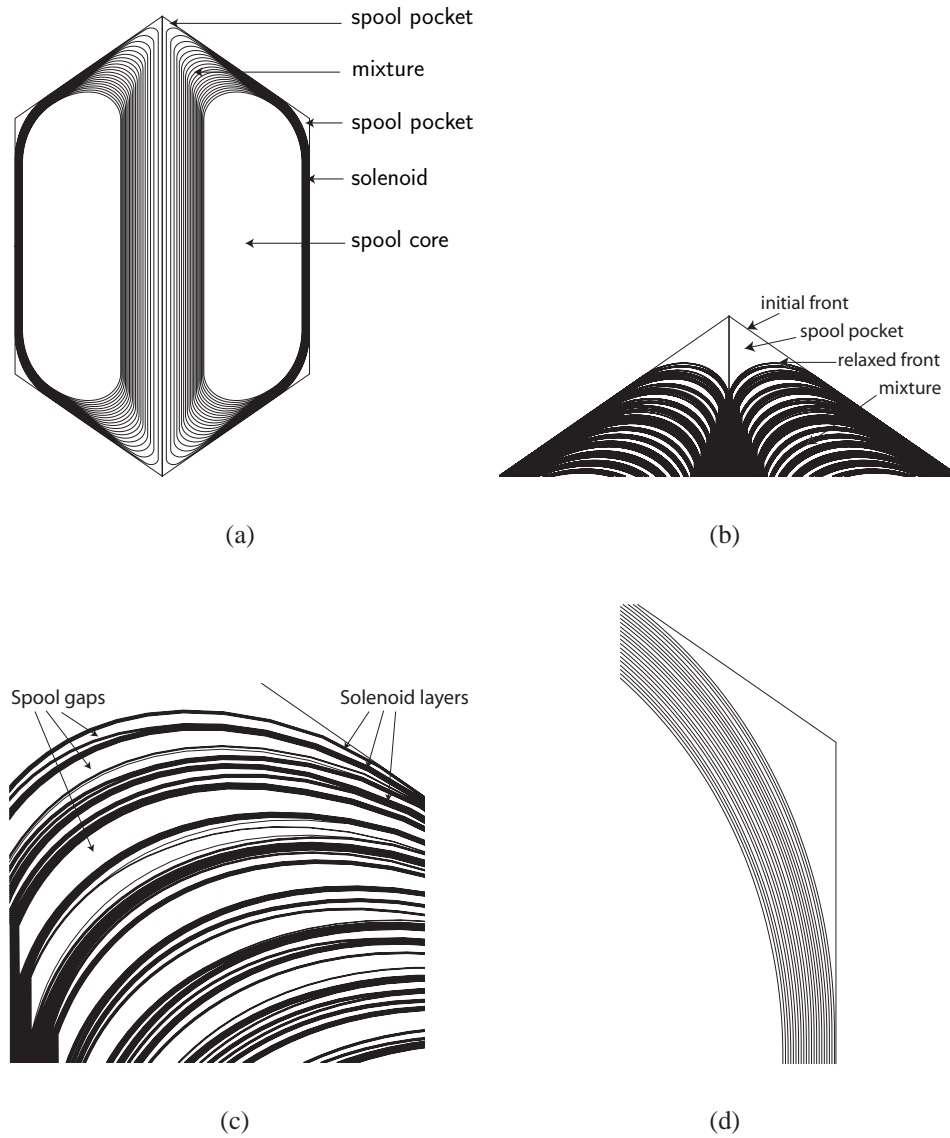


Figure 3.12: a) DNA conformation within a $\phi 29$ bacteriophage predicted by the mixed solenoid/spool construction. The conformation contains a solenoid/spool mixture region near the apices; spool pockets near the apices and shoulder of the capsid; and a spool core. b) Closeup of the apex of the capsid. c) Closeup of the solenoid/spool mixture at the apex of the capsid, consisting a of complex arrangement of alternating solenoid bundles and spool gaps. d) Closeup of the shoulder of the capsid, showing the relaxation of the initial front toward an equilibrium interface, the intervening spool gap, the subsequent solenoid bundle, and the spool core.

a fine solenoid/spool mixture develops near the apices, with the remainder of the front advancing in the solenoid phase. The latter phase has three regions where the DNA is straight: one along the axis of the capsid, and two abutting on the boundary of the capsid, joined by the curved transition shown in Figure 3.12d. This geometry tends to minimize the bending energy of the DNA, which confers on the structure an energetic advantage. Closeups of the solenoid/spool mixture at one of the apices of the capsid are shown in Figs. 3.12b,c. As may be seen from these figures, the mixed region consists of intricately interwoven solenoid bundles and spool gaps. The high degree of complexity of the DNA arrangement in this region is particularly noteworthy. The net energy reduction relative to the inverse spool construction is $\Delta E = -8.82 \times 10^3 \text{ pN} \times \text{nm}$, or roughly 11.8% of the total work required to pack the entire genome experimentally estimated by Smith et al. (2001) and a factor of six improvement over the circular solenoid evaluated in Section 3.2, which confers on the mixed solenoid/spool construction a non-negligible energy advantage over the inverse spool construction.

It should be noted that the fineness of the solenoid/spool mixture near the apices of the capsid is limited by the fineness of the discretization. Our numerical experiments indicate that increasing the resolution of the front tends to increase the fineness and complexity of the mixture. A plausible mathematical explanation for this behavior is that it may be but a manifestation of the lack of *lower-semicontinuity* of the energy functional and an instance of *non-attainment* (Dal Maso, 1993). Thus, the sequence of conformations obtained by applying the construction with increasing resolution, while exhibiting increasingly fine structure, is likely to generate well-defined probability measures in the limit. In particular, the volume fractions χ and $1 - \chi$ of the solenoid and spool phases, respectively, are likely to be well defined in the limit and to be in the interval $(0, 1)$. However, it was found earlier that minimizers alternate layers of pure phase, corresponding to either $\chi = 0$ or $\chi = 1$. Under these conditions, while the construction might indeed deliver a minimizing sequence of conformations, the (weak) limit of the sequence would not be a minimizer, which would exhibit the lack of lower-semicontinuity of the energy functional and the non-attainment of its infimum.

3.4 Summary

In this chapter we have used the director-field theory of Chapter 2 to study two low-energy *constructions* which model the packaged genome of a bacteriophage. With adoption of the popular *inverse spool* model, the director-field theory predicted with good accuracy the force vs. packing fraction relationship for the $\phi 29$ bacteriophage measured experimentally by Smith et al. (2001). In addition, the theory illuminated some interesting connections between the inverse spool packing hypothesis and the shapes of DNA condensates in the presence of polyvalent cations. On the other hand, the introduction of the torsionless toroidal solenoid model showed that the the inverse spool can be beaten at the game of energy minimization. Notably, a combination or mixture of the spool and solenoid configurations is able to achieve a significantly lower energy than either of the two pure phases. The question arises whether the solenoid configuration (either pure, or mixed with the spool) would be kinetically favorable. Clearly the theory in its current form is not capable of answering such questions.

Possibly the most important insight of this chapter is that the inverse spool is not necessarily the lowest energy configuration of the packaged genome. We are, therefore, increasingly motivated to search for other possible configurations of even lower energy. However, we would like not to be limited only to configurations suggested by our imaginations. It would be ideal to search in a more efficient and systematic manner for good configurations. One way to do this is to discretize the problem in order to search for finite dimensional approximate configurations. Chapter 4 does exactly that, resorting to methods of global numerical optimization to search for low-energy packing states.

Chapter 4

Numerical Optimization

This chapter considers spatial discretization of the DNA packaging problem. By introducing a finite-difference discretization, we transform the problem from one of the calculus of variations to one of *global numerical optimization*. We seek packing conformations which minimize a total energy *objective function* which has as its domain, director field values at a discrete set of positions on a Cartesian grid/lattice.

As previously remarked, the minimization problem (2.2.23) has a functional (2.2.22) with a nonconvex integrand. The implications of this fact are that the problem may possess many local minima, and indeed the global minimum may not be unique (see, e.g., Dacorogna, 1989). Consequently the discrete analog of problem (2.2.23) will target the minimization of a nonconvex total energy objective function. Such objective functions are typically described in terms of an “energy landscape” consisting of peaks, valleys, plateaus, etc. We do not have, at the outset, much intuition about the structure of the landscape, i.e., the numbers, heights, depths, and widths of hills and valleys. Hence, we need an optimization approach which can explore the landscape with robustness and efficiency.

For the discrete minimization problem, two optimization algorithms are employed: *simulated annealing* (SA) and the *nonlinear conjugate gradient* method (CG). The former is a stochastic optimization tool adept at finding global minima of complicated, nonconvex, multi-well objectives. With SA, there is always a finite probability of taking an occasional “uphill” step (resulting in an increase in the objective function). Because of this, SA can avoid getting quickly trapped in the nearest local minima, and is thereby able to explore the domain of the objective function with substantial freedom. CG is more skilled at quickly



Figure 4.1: Diagram of an embedded computational grid model of a $\phi 29$ bacteriophage.

resolving nearby local minima, and is considered a “greedy” optimization method, as it is designed to always choose changes to the system which lead to decreases in the objective function. We will exercise these two methods in conjunction to search for discrete energy minimizing DNA conformations.

The chapter begins by discretizing the theory of Chapter 2, thereby formulating the objective function and related numerical optimization problem. Following is a brief review of the two aforementioned numerical methods. Then, in order to gain some initial insight into the discrete problem, we optimize the DNA over the space of two-dimensional, planar configurations. Finally, we optimize the full three-dimensional lattice model.

4.1 Discrete problem

We discretize the problem by computing all field quantities of interest at points on a regular Cartesian grid (lattice). Let the position on this lattice be denoted by indices in parentheses (i, j, k) . For example, $m(i, j, k)$ gives the value of the director field at the lattice site corresponding to positions i , j , and k , respectively, along the three grid axes. Given this discretization, the integral constituting the free energy in (2.2.22) becomes a sum over the

lattice sites:

$$E = \sum_{i,j,k} \{W(i, j, k) + \phi(i, j, k)\} \Delta V \quad (4.1.1)$$

where $W(i, j, k)$ and $\phi(i, j, k)$ denote the strain energy and cohesive energy densities of (2.2.1) and (2.2.6), each evaluated using the values of the director field and its gradients at lattice site (i, j, k) . $\Delta V = \Delta x \Delta y \Delta z$ is the volume of each lattice cell, with Δx , Δy , and Δz being the grid spacings in each of the three lattice dimensions. Similarly, the total length integral in (2.2.23d) becomes

$$L = \sum_{i,j,k} |\mathbf{m}(i, j, k)| \Delta V. \quad (4.1.2)$$

The gradients of the director field needed for the computation of $W(i, j, k)$ can be approximated by finite differences. In particular, we choose the first-order central difference operator for points in the interior, i.e.,

$$\mathbf{m}_{,x} \approx \frac{\mathbf{m}(i+1, j, k) - \mathbf{m}(i-1, j, k)}{2\Delta x} \quad (4.1.3)$$

$$\mathbf{m}_{,y} \approx \frac{\mathbf{m}(i, j+1, k) - \mathbf{m}(i, j-1, k)}{2\Delta y} \quad (4.1.4)$$

$$\mathbf{m}_{,z} \approx \frac{\mathbf{m}(i, j, k+1) - \mathbf{m}(i, j, k-1)}{2\Delta z}, \quad (4.1.5)$$

applying the operator recursively to obtain higher gradients. For boundary points we use the corresponding forward difference operator,

$$\mathbf{m}_{,x} \approx \frac{\mathbf{m}(i+1, j, k) - \mathbf{m}(i, j, k)}{\Delta x} \quad (4.1.6)$$

$$\mathbf{m}_{,y} \approx \frac{\mathbf{m}(i, j+1, k) - \mathbf{m}(i, j, k)}{\Delta y} \quad (4.1.7)$$

$$\mathbf{m}_{,z} \approx \frac{\mathbf{m}(i, j, k+1) - \mathbf{m}(i, j, k)}{\Delta z}, \quad (4.1.8)$$

or backward difference operator

$$\mathbf{m}_{,x} \approx \frac{\mathbf{m}(i, j, k) - \mathbf{m}(i - 1, j, k)}{\Delta x} \quad (4.1.9)$$

$$\mathbf{m}_{,y} \approx \frac{\mathbf{m}(i, j, k) - \mathbf{m}(i, j - 1, k)}{\Delta y} \quad (4.1.10)$$

$$\mathbf{m}_{,z} \approx \frac{\mathbf{m}(i, j, k) - \mathbf{m}(i, j, k - 1)}{\Delta z}, \quad (4.1.11)$$

as is appropriate.

The objective function targeted for minimization is the free energy sum (4.1.1), and the unknowns of the problem are the N lattice-site values of the director field, $\mathbf{m}(i, j, k)$, which form a space of $3N$ continuously real-valued parameters. These parameters must obey discrete versions of constraints (2.2.23b)–(2.2.23d). Thus the numerical optimization problem is

$$\min_{\mathbf{m}(i,j,k)} E = \sum_{i,j,k} \{W(i, j, k) + \phi(i, j, k)\} \Delta V \quad (4.1.12a)$$

$$\text{subject to: } \nabla \cdot \mathbf{m}(i, j, k) = 0 \quad \text{in } \Omega \quad (4.1.12b)$$

$$\mathbf{m}(i, j, k) \cdot \boldsymbol{\nu}(i, j, k) = 0 \quad \text{on } \partial\Omega \quad (4.1.12c)$$

$$\sum_{i,j,k} |\mathbf{m}(i, j, k)| \Delta V = L. \quad (4.1.12d)$$

4.1.1 Constraints

Of the three constraints in (4.1.12), two are local (4.1.12b, 4.1.12c) and one is global (4.1.12d). Because (4.1.12b) is active at all points in the discretization, we view it as the highest priority constraint, letting our strategy for enforcement of this constraint dictate the way we handle the other two. Fortunately, this constraint may be trivially enforced by the introduction of a vector potential (call it the *director potential*), denoted by \mathbf{v} , defined such that

$$\mathbf{m} = \text{curl}(\mathbf{v}) \equiv \nabla \times \mathbf{v}. \quad (4.1.13)$$

Satisfying the divergence constraint in this way, we redefine the optimization problem in terms of the lattice-site values of the director potential, $\mathbf{v}(i, j, k)$, which become the primal unknowns.

This choice clearly affects the way we enforce (4.1.12c) and (4.1.12d). Had we been able to enforce (4.1.12b) without changing the primal unknown, (4.1.12c) would have allowed for straightforward enforcement (simply by removing any component of \mathbf{m} not tangent to the boundary). However, by introducing the vector potential, the boundary condition is now a constraint on the gradient of the primal field at the boundary. This is more difficult to enforce point-wise. Given this difficulty and the fact that (4.1.12d) is a global constraint, a reasonable strategy is to choose weak enforcement for both constraints via a penalty method. By an appropriate choice of the penalty parameter, this method can shrink any constraint violations to within an arbitrary tolerance. For some proofs of convergence and a nice discussion of penalty methods, see (Luenberger, 1989).

4.1.2 Minimization problem

Following the penalty approach, we formulate a new objective function:

$$I(\epsilon_1, \epsilon_2, \mathbf{v}(i, j, k)) = \tilde{E}(\mathbf{v}(i, j, k)) + \frac{1}{2\epsilon_1} P_1(\mathbf{v}(i, j, k)) + \frac{1}{2\epsilon_2} P_2(\mathbf{v}(i, j, k)), \quad (4.1.14)$$

where

$$\tilde{E}(\mathbf{v}(i, j, k)) = E(\text{curl}(\mathbf{v}(i, j, k))) \quad (4.1.15)$$

is the energy as a function of the director potentials;

$$P_1(\mathbf{v}(i, j, k)) = \sum_{(i,j,k) \text{ on } \partial\Omega} [\mathbf{m}(i, j, k) \cdot \boldsymbol{\nu}(i, j, k)]^2 \quad (4.1.16)$$

$$P_2(\mathbf{v}(i, j, k)) = \left[L - \sum_{i,j,k} |\mathbf{m}(i, j, k)| \Delta V \right]^2 \quad (4.1.17)$$

are the penalty functions corresponding to constraints (4.1.12c) and (4.1.12d), respectively; and ϵ_1 and ϵ_2 are two numbers chosen small enough to satisfy the constraints to within an

arbitrary tolerance. This leads to a new, approximate but unconstrained version of the optimization problem:

$$\min_{\mathbf{v}^{(i,j,k)}} I(\epsilon_1, \epsilon_2, \mathbf{v}^{(i,j,k)}). \quad (4.1.18)$$

This unconstrained optimization problem is in a form amenable to treatment by SA and CG.

4.2 Numerical methods

We briefly describe the numerical optimization methods which are used in the analysis to follow.

4.2.1 Simulated annealing

Simulated annealing (SA) is a stochastic or *Monte Carlo* method for global optimization based on an analogy to the slow cooling of a thermodynamical physical system. As its name betrays, SA mimics the physical process of annealing, in which a material (e.g., steel), initially at high temperature (where the material is soft and its constitutive atoms are fairly free to move around), is slowly brought to room temperature (where the atoms are more tightly constrained). If the process is done sufficiently slowly, the material is able to maintain statistical or thermodynamic equilibrium (having the lowest possible free energy) at all temperatures. This is in contrast with quenching, wherein the material is quickly brought from high to low temperature, increasing the likelihood that it will be “frozen” in a non-equilibrium state (with higher free energy) at the final temperature. SA mimics this process by performing a random walk through the state space (domain) of the objective function, controlling fluctuations in the objective via a parameter identified as the fictitious temperature T . Just as in a physical annealing process, T starts high, allowing initially large fluctuations, and is slowly lowered in time according to some *annealing schedule*, denoted $T(t)$, where t is algorithmic time, i.e., the number of iterations of the algorithm that have been performed. For example, two of the more popular schedules are the *exponential* schedule, $T(t) = T_0 \alpha^t$, $\alpha \in (0, 1)$, and the *linear* schedule, $T(t) = T_0 - \alpha t$.

In general, every SA algorithm is a repetition of the following steps:

1. Propose a new state x' for the system by applying some random change Δx to the current state x of the system:

$$x' = x + \Delta x$$

2. Decide whether to move the system to the newly proposed state x' or to stay at the current state x .

Following Salamon et al. (2002), the generator of the new trial states in step 1 above will be referred to as a *move class*, and the criterion for moving to a new state in step 2 will be referred to as the *acceptance criterion*. The acceptance criterion is always based in some way on the current temperature and the move's energy cost (or savings) such that increases in energy are more seldom accepted as temperature drops. The most frequently used acceptance criterion is that of Metropolis et al. (1953), where the probability of acceptance is given by

$$P_{\text{met}}(\Delta E) = \begin{cases} 1, & \text{if } \Delta E \leq 0 \\ e^{-\Delta E/T}, & \text{if } \Delta E > 0. \end{cases} \quad (4.2.1)$$

Clearly the Metropolis criterion always accepts downhill moves, and accepts uphill moves with a probability which decreases with increasing size of the uphill move and decreasing temperature. In general, the move class can also be influenced by the annealing schedule. This can be handy for problems (like the present one) in which the unknowns in state space can take on a continuum of values. In such cases it may be desirable to attempt larger moves at high temperature, and smaller moves at low temperature.

The original version of SA (Kirkpatrick et al., 1983) derived its acceptance criterion from the Metropolis algorithm (Metropolis et al., 1953), while decreasing temperature exponentially in time. Many other specific variants of SA have been used and proposed, each differing from the others in the choices of annealing schedule, move class, and acceptance criterion.

Experimenting with these choices on the present problem has made clear the need for a move class which depends on temperature. Algorithms which attempt larger moves at high

temperature and smaller moves at low temperature appear to be more efficient than those attempting moves of uniform distance. One such approach is *fast simulated annealing* (FSA) (Szu and Hartley, 1987). The move class for this approach generates changes to the state having a Cauchy distribution centered at zero. The probability density of this distribution is

$$P_{gen}(x) = \frac{1}{\pi} \frac{T_{gen}}{T_{gen}^2 + x^2}, \quad (4.2.2)$$

where T_{gen} is a temperature parameter which controls the width of the distribution. The Cauchy distribution is noteworthy in that its peak is very similar in shape to a Gaussian, but its tails are much wider and decay much more slowly than those of a Gaussian. Hence, most proposed moves will be small and local (not far from the peak). But because of the wide tails, very large moves will occasionally be proposed, improving the likelihood of occasionally jumping from the neighborhood of one local minimum to another, often improving the efficiency of the annealing. Moves are accepted with probability

$$P_{acc}(\Delta E) = \frac{1}{1 + \exp(\Delta E/T)} \quad (4.2.3)$$

where the system temperature varies according to an annealing schedule which is inversely linear in time

$$T(t) = T_0/(1 + t). \quad (4.2.4)$$

Typically, the state generation temperature T_{gen} is proportional to the acceptance temperature T , such that the characteristic move size and the acceptance probability decrease according to the same annealing schedule. This too increases the efficiency of the algorithm, avoiding an abundance of moves which are always too large to be accepted at the final stages of cooling.

The annealing algorithm used in the present work is identical to FSA with one exception: the annealing schedule is slightly slower than that of straight-forward FSA. The acceptance temperature is cooled according to Equation (4.2.4), but at each t , the system is allowed to obtain a partial equilibrium by attempting a number of moves at fixed temperature. This number of moves, N , is set to be on the order of the dimension of the system.

Annealing schedules which are faster than this (e.g., the exponential schedule, also referred to as “quenching”) get stuck in local minima too easily. FSA with partial equilibration is the most efficient (i.e., achieving the lowest minimum in the shortest time) of all of the annealing algorithms tested.

4.2.2 The nonlinear conjugate gradient method

The nonlinear conjugate gradient method (CG) is used to extremize the objective function (4.3.6) *locally* by driving its gradient, i.e., the vector of derivatives with respect to grid point values of the director potential $\partial I / \partial v(i, j, k)$, to zero. By carefully ensuring that all steps taken by the algorithm lead “downhill”, i.e., to lower values of the objective, this method can (quickly) locate a local minimum. The specific flavor of nonlinear CG used is the Polak-Ribiere method with a line search satisfying the strong Wolfe conditions. Rather than provide details here, we refer to Nocedal and Wright (1999) for a lucid description of the CG and line search methods.

Since CG is a very “greedy” method, it will almost always identify the local minimum closest to the starting point in state space. If there is to be any hope of using CG effectively on the bacteriophage DNA packaging problem, it hangs on the judicious choice of a starting point. The choice made here is to use low energy states identified by simulated annealing as starting points for CG. In this context, nonlinear CG can be viewed as a refinement tool to be applied in cooperation with SA. An unfortunate property of the SA algorithm implemented for this work is that the annealing can become less efficient once it has found the spool region of state space, achieving smaller and smaller improvements in the minimum energy as the temperature sinks lower. A nice strategy, then, is to stop the annealing algorithm when it seems to have reached a low energy basin, and use nonlinear CG to find the bottom of that basin. If the results of the annealing do not actually correspond to a basin, but instead a long, narrow valley or some other shaped region in state space, the CG with Wolfe line search should be robust enough to detect it.

4.3 Optimization in two dimensions

As a first step in an incremental advance on the general problem of (4.1.18), consider the restriction of the director field to the plane (say, the x - y plane). Consistent with a planar director field is a director potential of the form

$$\mathbf{v}(\mathbf{x}) = \{0, 0, v(x, y)\} \quad (4.3.1)$$

such that

$$\mathbf{m} = \begin{Bmatrix} v_{,y} \\ -v_{,x} \\ 0 \end{Bmatrix}. \quad (4.3.2)$$

Note that the director field has the interpretation of a 90° rotation of the 2-D gradient of the potential. Thus, the 2-D restriction permits an intuitively simple enforcement of boundary condition (4.1.12c) in terms of v . If \mathbf{m} is to be tangent to the boundary, then the gradient of v should be normal to the boundary. So clearly the constraint is satisfied exactly if v has a constant value (say, zero) along the boundary:

$$v = 0 \quad \text{on } \partial\Omega. \quad (4.3.3)$$

Enforcing the boundary condition thusly, we can avoid the boundary penalty term for the 2-D case.

Since the director field is planar, torsion is identically zero, and the total energy is comprised only of elastic energy due to bending and interaction energy

$$E(\mathbf{m}, \nabla \mathbf{m}) = h \int_{\omega} \frac{A}{2} \kappa^2 |\mathbf{m}| + \phi(|\mathbf{m}|) dx dy \quad (4.3.4)$$

where h is the height of the capsid and ω is the area in the plane occupied by DNA. A simple calculation shows that the curvature is given in terms of v by the expression

$$\kappa^2 = |\mathbf{t} \cdot \nabla \mathbf{t}|^2 = (v_{,xx} v_{,y}^2 - 2v_{,x} v_{,y} v_{,xy} + v_{,yy} v_{,x}^2)^2 / |\mathbf{m}|^6. \quad (4.3.5)$$

Note that, since the height of the cylindrical capsid h is everywhere a constant factor, we can normalize all integrals/sums by h for simplicity. As in the previous section, discretization converts integrals to sums and we have

$$I(\epsilon, v(i, j)) = E(v(i, j))/h + \frac{1}{2\epsilon}P(v(i, j)) \quad (4.3.6)$$

$$E(v(i, j))/h = \sum_{i,j} \{W(i, j) + \phi(i, j)\} \Delta A \quad (4.3.7)$$

$$P(v(i, j)) = \left[L/h - \sum_{i,j} |m(i, j)| \Delta A \right]^2, \quad (4.3.8)$$

with $\Delta A = \Delta x \Delta y$ giving the area of each 2-D lattice cell. The 2-D minimization problem is

$$\min_{v(i,j)} I(\epsilon, v(i, j)). \quad (4.3.9)$$

4.3.1 Bacteriophage $\phi 29$

FSA has been used to optimize (4.3.6) over a circular cross section of a cylinder model of a $\phi 29$ bacteriophage. 2-D packing of the full $\phi 29$ genome of length 6600 nm is optimized. The cylinder model is 40 nm in diameter and 40 nm in height (dimensions which give approximately the capsid volume of $\phi 29$). The spatial domain is discretized with a regular Cartesian grid having 20 points per side. Circular geometry is approximated by “cutting off corners” of the grid, i.e., neglecting grid points distanced farther from the center than the desired radius. The initial state for annealing simulations consisted of random values for the director potential $v \in [-\ell, \ell]$, where ℓ is a length parameter consistent with the dimensions of the capsid.

Annealing schedule. To determine the appropriate annealing schedule, 20 randomly initialized systems were annealed with initial temperatures in the ranges $T_0 \in [10, 10^5]$ and $(T_0)_{\text{gen}} \in [10^{-3}, 10]$. The annealing was terminated after a total of 4×10^7 generation steps, at which time, most of the systems seemed fairly well equilibrated. As is evident from

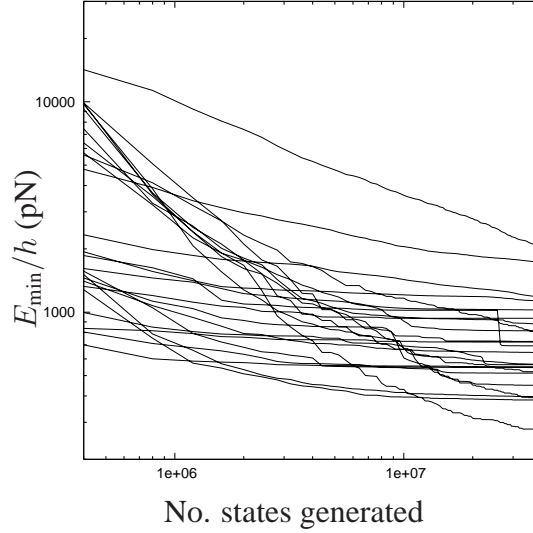
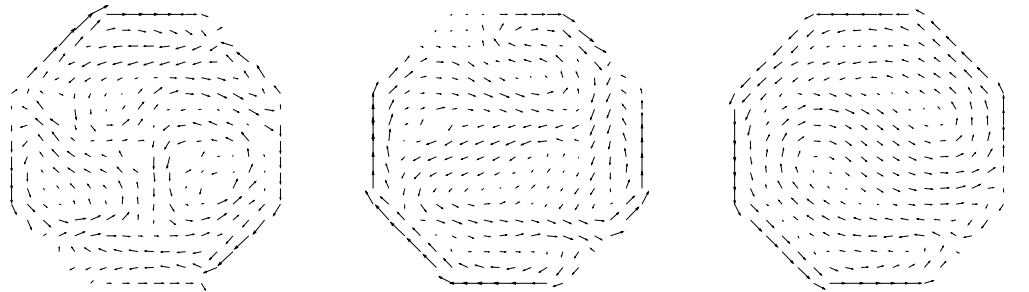


Figure 4.2: Log-log plot of the height-normalized minimum energy, E_{\min}/h vs. the number of trial states generated by the annealing algorithm.

Figure 4.2, certain initial temperatures produced better annealing trajectories than the rest. Specifically the choice: $T_0 = 10^5$ and $(T_0)_{\text{gen}} = 1$ yielded the lowest minimum energy.

Figure 4.3 shows a few representative final configurations produced by the different temperature schedules. Note the last two configurations shown in Figure 4.3d,e. These show the first evidence of the energy minimizing character of the spool motif. Figure 4.3d is not quite perfectly spooled, due to an eddy near its middle right boundary. This small eddy leads to a slightly higher energy than the nearly ideally spooled result in Figure 4.3e. These “temperature trials” suggest that initial temperatures of approximately $T_0 = 10^5$ and $(T_0)_{\text{gen}} = 1$ should give optimal results with reasonable efficiency (i.e., we don’t have to wait forever for the answer). We note that at these initial temperatures, any bias that the initial state has for a certain configuration is quickly erased in the initial steps of the random walk. Therefore, in all subsequent annealing calculations, every system is arbitrarily initialized with the vector potential everywhere equal to zero.

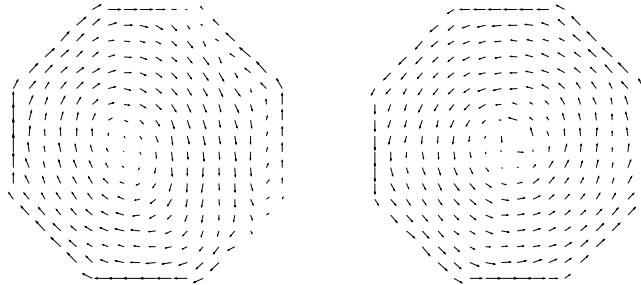
“Shotgun” annealing. At initial temperatures $T_0 = 10^5$ and $(T_0)_{\text{gen}} = 1$, equilibrium fluctuations are large enough that initial conditions are irrelevant. Using a “shotgun parallelism” approach, multiple duplicate systems were simultaneously annealed on a 62-node Linux cluster of 64-bit Compaq Alpha processors. Each annealing was allowed to proceed



(a) $T_0 = 10^2$; $(T_0)_{\text{gen}} = 1$;
 $E/h = 716.159$ pN

(b) $T_0 = 10^3$; $(T_0)_{\text{gen}} = 1$;
 $E/h = 546.024$ pN

(c) $T_0 = 10^4$; $(T_0)_{\text{gen}} = 1$;
 $E/h = 397.134$ pN



(d) $T_0 = 10^5$; $(T_0)_{\text{gen}} = 10$;
 $E/h = 386.138$ pN

(e) $T_0 = 10^5$; $(T_0)_{\text{gen}} = 1$;
 $E/h = 272.133$ pN

Figure 4.3: Several of the configurations produced in the annealing “temperature trials.”

for 240 million steps (an order of magnitude longer than the time trials discussed above) to ensure equilibration. Each annealed configuration was easily identifiable as belonging qualitatively in one of two groups:

1. *Perfect Spool*: Director field is nearly exactly circumferential everywhere. Figure 4.3e exemplifies this configuration.
2. *Imperfect Spool*: Almost the same as the perfect spool, except for a single boundary eddy, i.e., a region of recirculation of the director field adjacent to the boundary. Figure 4.3d exemplifies this configuration.

In all cases, the perfect spool attains a lower energy (typically $\sim 50\%$ lower) than the imperfect spool. Figure 4.4a shows the single conformation with the lowest energy attained in the battery of annealing runs. Figure 4.4b shows the same conformation after further optimization with CG. Apparent from the figures, CG has only a very minimal smoothing effect on the SA result. The CG-smoothed result shows the DNA density (vector field length) to be more uniform throughout the capsid except for an inner core where the density (and vector field) drop to zero.

Curious, one might think, is the fact that the total energy of the CG-smoothed conformation is actually slightly higher than the unsmoothed SA conformation ($E/h = 284.223$ pN *vs.* $E/h = 223.619$ pN). We believe this is a numerical pathology associated with the zero-density limit, $u \rightarrow 0$. Note that in the 2-D case the density is equal to the magnitude of the 2-D gradient of the scalar director potential, $u = |\nabla v|$. Thus, in the case where $\nabla v \rightarrow 0$ faster than $\nabla \nabla v \rightarrow 0$, the expression for the square of the curvature (4.3.5) can blow up numerically as the numerator goes as $\mathcal{O}(|\nabla v|^4)$ and the denominator goes as $\mathcal{O}(|\nabla v|^6)$. To avoid this degeneracy, the numerical implementation maintains a minimum-density tolerance. Whenever this tolerance is violated, the density and curvature are set to zero. As a result, the objective function as implemented is actually discontinuous! It is interesting that the SA algorithm is able to take advantage of this pathology, finding a lower energy than the CG method in the same close neighborhood. However, given that the CG algorithm quickly moved to an apparently smoother part of the neighborhood, it is reasonable to conjecture that its solution more closely reflects the original problem.

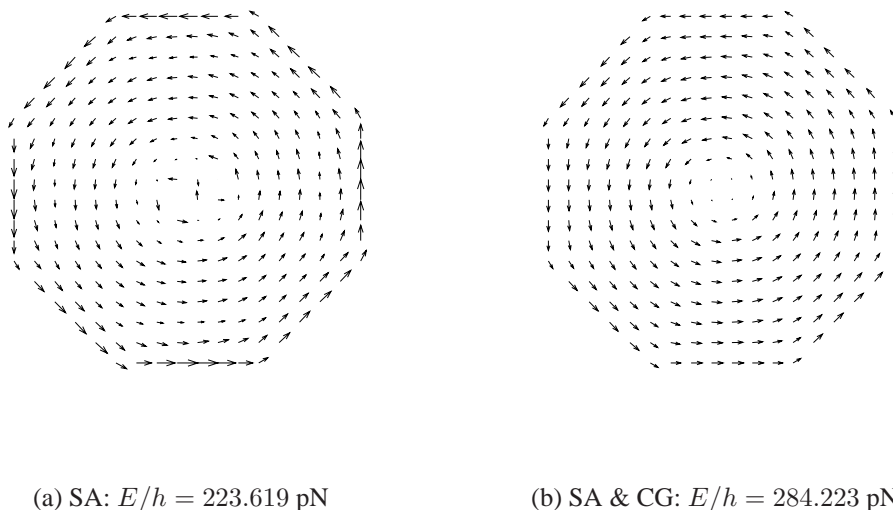


Figure 4.4: Lowest-energy 2-D conformation. (a) Conformation attained with FSA. (b) Annealed conformation after further optimization with CG.

In summary, these results strongly suggest that the so-called *inverse spool* configuration is a global minimizer for the 2-D problem.

4.4 Optimization in three dimensions

The optimization results of Section 4.3 strongly suggested that the so-called *inverse spool* configuration is a global minimizer when the problem is restricted to two dimensions. Motivated by these findings, we choose to perform a full 3-D optimization with the inverse spool as the starting point. If the spool is, in fact, the 2-D minimizer, a number of questions are raised by expanding to three dimensions: Is the inverse spool also a (local) minimizer in the full 3-D case? If so, then is it also a global minimizer? If not, what are the closest (local) minima in the neighborhood of the inverse spool? It is clear, then, that the inverse spool would be a very interesting starting point for a CG analysis. Nonlinear CG can help to answer the question of whether or not the inverse spool is an equilibrium state. If it is, CG will converge immediately as stationarity implies a zero gradient. If it is not, CG will

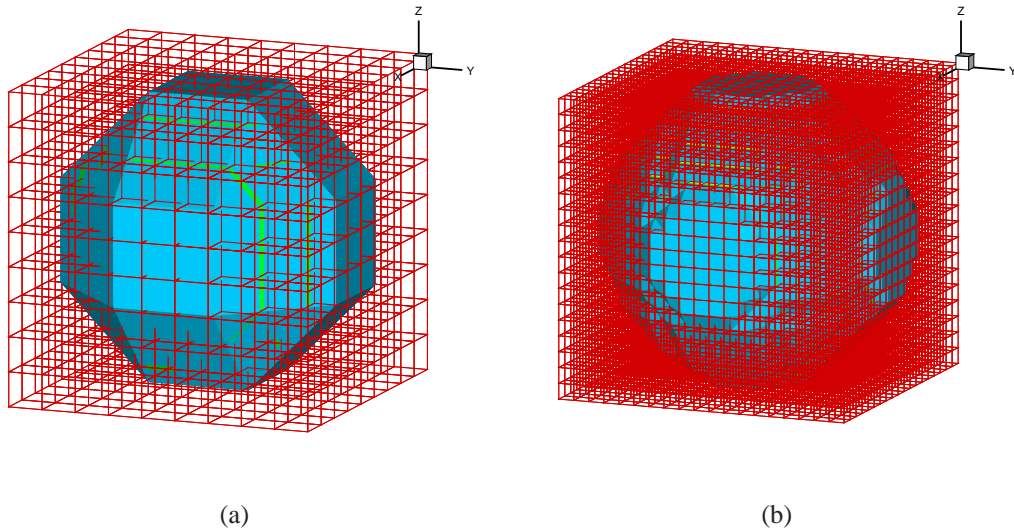


Figure 4.5: Lattice models of a bacteriophage λ : (a) 10 points per edge, (b) 20 points per edge

go (downhill) in search of the nearest local minimum. As already discussed, SA would be a good candidate to search more widely for the global minimum, which in theory, could be very far away from the inverse spool in state space. In the following, both of these methods are applied in the effort to answer the above questions.

As a case study for 3-D optimization, we choose to model bacteriophage λ . Its icosahedral capsid is modeled as a sphere of radius $R = 27.5$ nm, and its genome has length $L = 16.5$ μm (Kindt et al., 2001). Two cubic computational lattices are used: one with 10 grid points per edge, and a second with 20 grid points per edge, as shown in Figure 4.5.

4.4.1 Simulated annealing

Fast simulated annealing was performed on spool-initialized configurations for both the 10-point and 20-point lattices shown in Figure 4.5. The 10-point lattice model was annealed for 5 million steps from initial temperatures of $T_0 = 10^5$ and $(T_0)_{\text{gen}} = 0.1$. The 20-point lattice model was annealed for 50 million steps from the same initial temperatures of $T_0 = 10^5$ and $(T_0)_{\text{gen}} = 0.1$. Though each system underwent enough rearrangement from the initial constant-density spool configuration to attain an energy drop of approximately 10%, at the

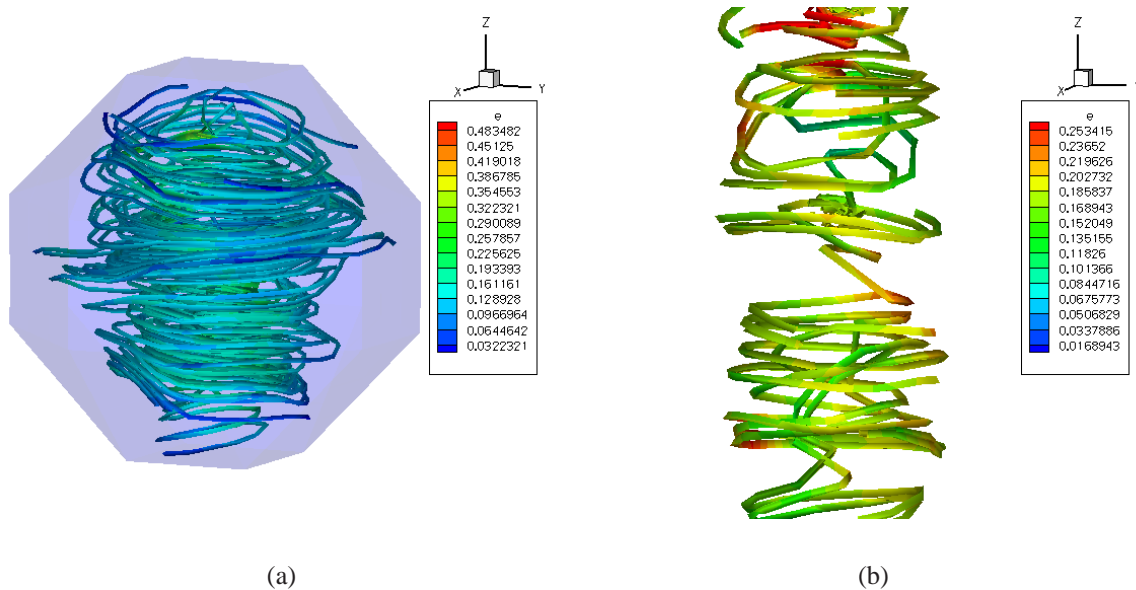


Figure 4.6: Results of FSA applied to spool configuration on 10-point-per-edge lattice: (a) Full view, (b) Closeup view of inner core. Ribbons are stream traces of the director field, indicating the direction of DNA at various positions within the capsid. Color indicates energy density.

gross qualitative level the spool configuration is retained. The annealed configurations are shown in Figures 4.6 and 4.7.

The most significant feature of the annealed configurations is that the director field has traveled out of the spooling plane. This is especially true near the center of the capsid, where spooled DNA has started to coil helically with a non-negligible pitch, conceivably to alleviate a high bending energy penalty.

4.4.2 Conjugate gradients

The conjugate gradient method has been run to convergence on the 10-point and 20-point spooled virus models. Results are very similar to those of Section 4.4.1. As is evident from Figures 4.8 and 4.9, CG produces configurations which appear more regular than those of SA. However, similar features are evident: spooling is persistent everywhere except in the inner core region. This region is larger as predicted by the lower resolution 10-point lattice than it is for the 20-point lattice. In fact, the lower resolution model shows some

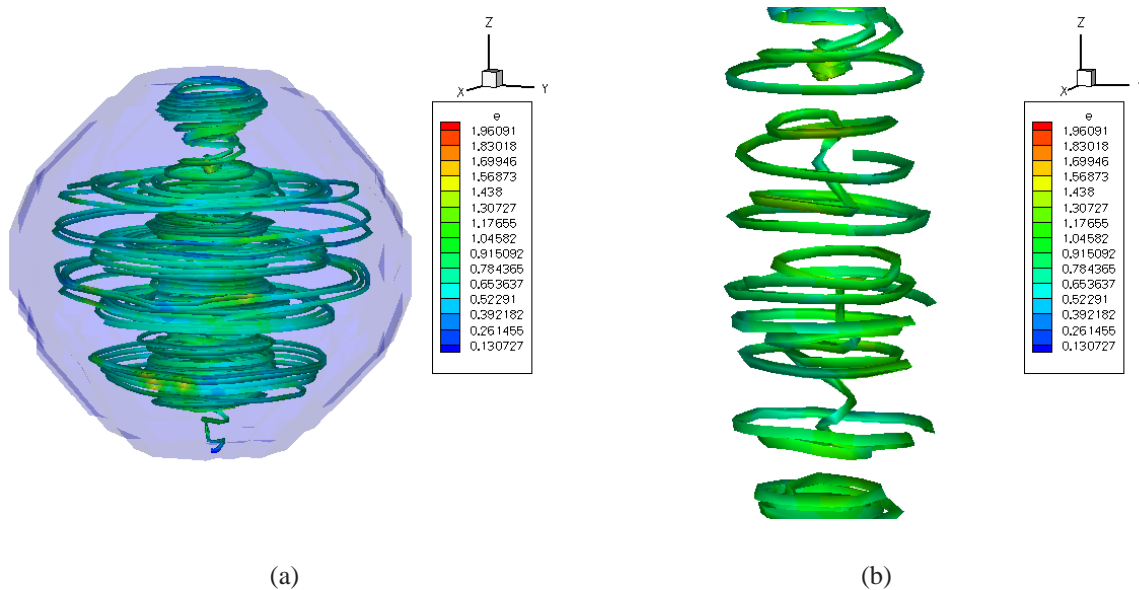


Figure 4.7: Results of FSA applied to spool configuration on 20-point-per-edge lattice: (a) Full view, (b) Closeup view of inner core. Ribbons are stream traces of the director field, indicating the direction of DNA at various positions within the capsid. Color indicates energy density.

out of spooling-plane motion of the director field even close to the boundary of the capsid. However, results at the two different resolutions are still qualitatively very much alike. By the inner core region with DNA having its direction pointing out of the spooling plane, the capsid is able to accommodate more DNA at a lower density without suffering a huge cost in bending energy. This is exactly what our mechanical intuition would suggest—that the spool would buckle once the curvature gets too high.

4.5 Summary

This chapter has developed a discretized director-field theory suitable for numerical computation. Given this theory, we have applied methods of numerical optimization to the virus packing problem. We have discovered that, by all indications, the inverse spool motif is the lowest energy conformation possible for planar DNA packaging. In addition, we have seen that, except for a small inner core region near the center axis of the virus, the

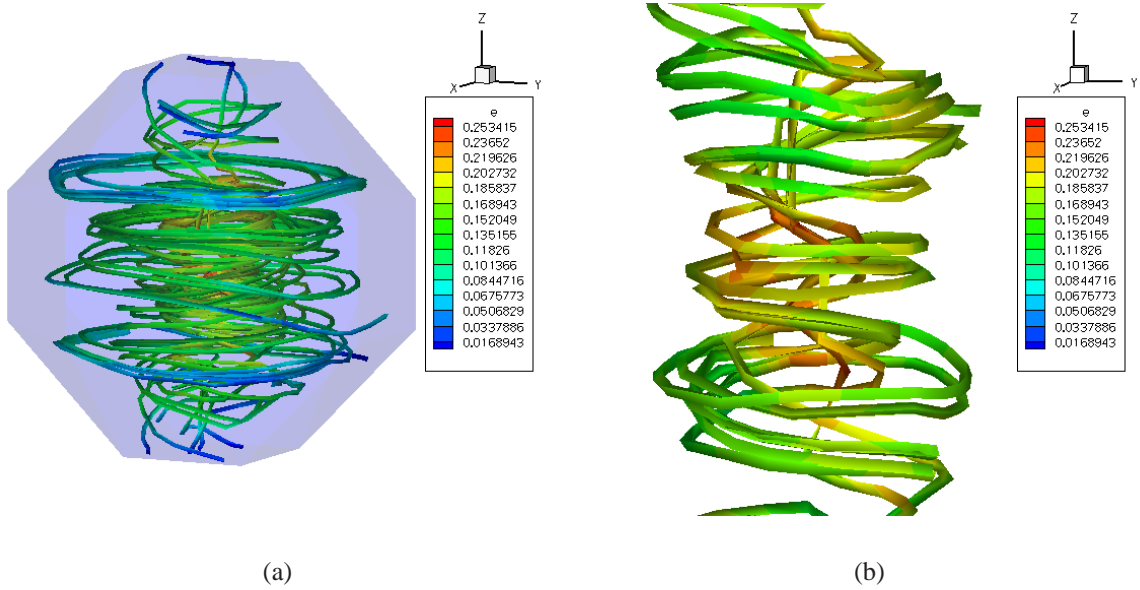


Figure 4.8: Results of CG applied to spool configuration on 10-point per edge lattice: (a) Full view, (b) Closeup view of inner core. Ribbons are stream traces of the director field, indicating the direction of DNA at various positions within the capsid. Color indicates energy density.

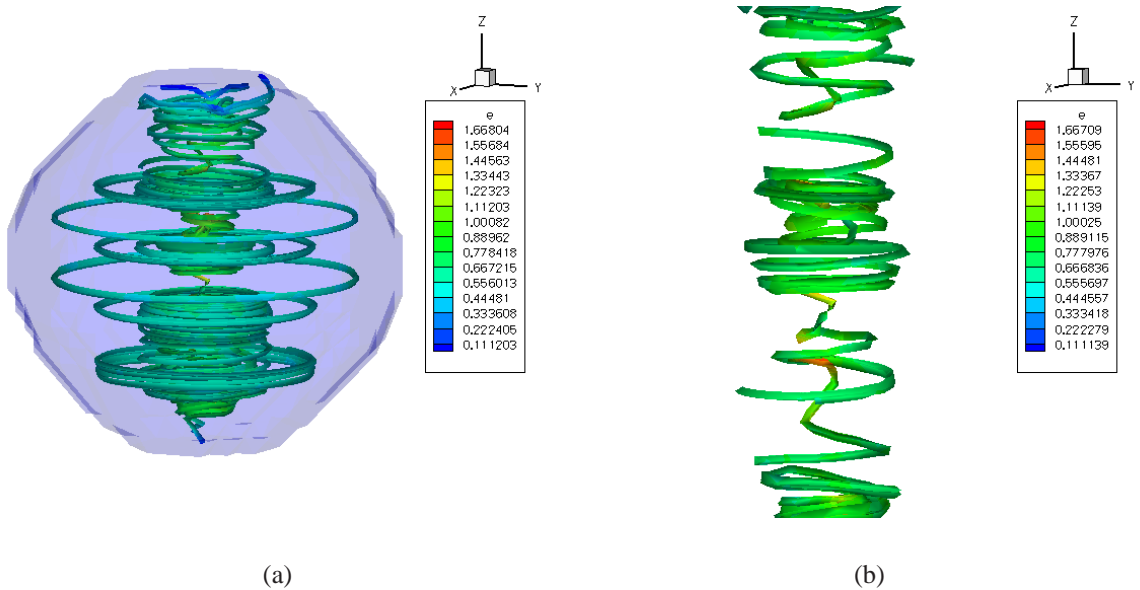


Figure 4.9: Results of CG applied to spool configuration on 20-point per edge lattice: (a) Full view, (b) Closeup view of inner core. Ribbons are stream traces of the director field, indicating the direction of DNA at various positions within the capsid. Color indicates energy density.

inverse spool is a stable configuration in three dimensions. DNA in the inner core has the tendency to buckle, coiling out of the spooling plane, most likely in order to alleviate high bending energy. Application of the method of simulated annealing gives us confidence that the buckled inverse spool is a fairly deep basin in the energy landscape—one which is much lower than any other in a sizable neighborhood.

Chapter 5

Conclusion

In this thesis we have developed a continuum model of encapsidated DNA in which the DNA conformations are described by means of a director field. The point values of the director field give the local direction and density of the DNA. Chapter 2 showed that it is possible to write down an energy functional accounting for bending, torsion, and electrostatic interaction solely in terms of the director field. Energy minimization, subject to a divergence constraint resulting from the continuity of the genome, selects the DNA conformations of interest.

Chapter 3 presented an analytical application of the theory to the $\phi 29$ bacteriophage, with the direct formulation of low-energy constructions. We studied extensively two constructions, the inverse spool and torsionless toroidal solenoids. Analysis of the inverse spool predicted a relationship between force and length packed which compares very well with experiment. Further, we showed that under the assumption of constant DNA density, torsionless toroidal solenoids, consisting of planar coils contained within meridional planes and wrapped around a spool core, and fine mixtures of the solenoid and spool phase, *beat* the inverse spool construction at the game of energy minimization.

In Chapter 4 we outlined a spatially discrete version of the theory presented in Chapter 2. With the formulation of a computational lattice model of DNA packaging we utilized methods of global numerical optimization to minimize the total energy. In two dimensions, the winning configuration was shown with little doubt to be the inverse spool. The lowest-energy 2-D configuration was a spool of fairly constant DNA density everywhere except at the center where an empty inner core was found having zero DNA density. Optimiza-

tion in three dimensions showed that the spool is fairly robust—energetically much more favorable than any nearby point in configuration space. More precisely, the lowest-energy 3-D configuration exhibited the spool motif everywhere except in a small inner core region about the central axis of the capsid. In this region the DNA had buckled out of the spooling plane such that the core was filled with DNA without suffering a high bending energy penalty.

As pointed out by Kindt et al. (2001), the direct elucidation of the statistical mechanics of a semi-flexible, highly-charged chain confined to a domain of dimensions comparable to its persistence length and orders of magnitude smaller than its total length constitutes a daunting theoretical challenge. The introduction of a director field greatly simplifies the analytical and numerical treatment of the problem, by reducing it to the minimization of a fairly concise energy functional. As already mentioned, the structure of the energy functional, and of the constraints that arise in the theory, is reminiscent of problems in micromagnetics (e.g., de Simone et al., 2000), and it is to be expected that much of the insight and experience which has been developed in that context might carry over to the present setting. For instance, the modulus constraint acting on the unit director field \mathbf{t} is *nonconvex* and, consequently, the constrained energy functional lacks lower semicontinuity. This has the far-reaching consequence that the infimum of the energy is not attained in general, although the energy may be driven arbitrarily close to its infimum by allowing for increasingly finer and more complex microstructure. We have observed what appear to be manifestations of this type of behavior in the mixed solenoid/spool construction, which leads to intricate arrangements of solenoid layers and spool gaps which grow in complexity as the resolution of the front is increased. This type of behavior suggests that much progress can be made by the application of weak convergence and variational calculus tools, such as relaxation and Γ -convergence (Dal Maso, 1993), but the elucidation of these issues is well beyond the scope of this thesis.

We conclude by pointing out some of the limitations of the present analysis, and possible future improvements. In formulating the energy functional, only limited attention was paid to interfacial energies. In particular, we neglected such energy as may be carried by solenoid/spool interfaces. Consideration of this source of energy introduces a length scale

into the problem, and may be expected to introduce a cut-off for the fineness of the DNA structure. We have also neglected the elasticity and strength of the capsid. A lucid discussion of these effects and a calculation of the limit pressure that a $\phi 29$ can sustain may be found in the recent work of Purohit et al. (2003).

The three-dimensional optimization presented in Chapter 4 could benefit from a less biased choice for the initial state. Not denying the importance of the buckled inverse spool as a novel packing motif, a more exhaustive annealing search for other local minimizers remains of high interest.

Finally, there are well-known limitations to the energy-minimization paradigm itself. Thus, in constructing low energy DNA conformations, no regard is given to whether those conformations can be attained through the gradual insertion of DNA into the capsid. In nature, there may be topological obstructions, not accounted for by the theory, which may impede the attainment of certain low-energy structures and promote metastability. Another important aspect of DNA packaging neglected in the theory is kinetics. In particular, the prediction of packaging rates is beyond the scope of the theory in its present form.

Appendix A

Configurational forces

While complete treatments of configurational forces for standard systems, such as elastic bodies, may be found in a number of sources (e. g., Gurtin (2000)), the systems of interest here deviate somewhat from the standard case in that the energy density depends on the second derivatives of the field, i.e., on the torsion, and the field must satisfy an internal constraint, namely, it must be divergence free. For completeness, in this appendix we provide a brief derivation of the configurational forces pertaining to the systems of interest.

The energy of the systems under consideration is of the general form

$$E(\mathbf{u}) = \int W(\mathbf{x}, \mathbf{u}(\mathbf{x}), D\mathbf{u}(\mathbf{x}), D^2\mathbf{u}(\mathbf{x})) dx, \quad (\text{A.0.1})$$

where $\mathbf{u} : \mathbb{R}^n \rightarrow \mathbb{R}^m$, $D\mathbf{u} = \{D^\alpha\mathbf{u}, |\alpha| = 1\}$ and $D^2\mathbf{u} = \{D^\alpha\mathbf{u}, |\alpha| = 2\}$. Since configurational forces at the boundary are of no immediate concern as regards the applications pursued in this work, we consider a system of infinite extent and extend all integrals to \mathbb{R}^n .

The variational problem is

$$\inf E(\mathbf{u}), \quad \text{subject to: } g(\mathbf{x}, \mathbf{u}(\mathbf{x}), D\mathbf{u}(\mathbf{x})) = 0 \quad \text{in } \Omega, \quad (\text{A.0.2})$$

where the function g represents an internal constraint of the system. The first variation of the energy is the functional

$$\delta E(\mathbf{u}, \mathbf{w}) = \int \left(\frac{\partial W}{\partial u_r} w_r + \frac{\partial W}{\partial u_{r,i}} w_{r,i} + \frac{\partial W}{\partial u_{r,ij}} w_{r,ij} \right) dx. \quad (\text{A.0.3})$$

Assuming sufficient regularity, the solutions of problem (A.0.2) satisfy the stationary condition

$$\delta E(\mathbf{u}, \mathbf{w}) = 0 \quad (\text{A.0.4})$$

for all admissible variations \mathbf{w} consistent with the internal constraints, i.e., such that

$$\frac{\partial g}{\partial u_r} w_r + \frac{\partial g}{\partial u_{r,i}} w_{r,i} = 0. \quad (\text{A.0.5})$$

Equivalently, the solutions satisfy the Euler-Lagrange equations:

$$\frac{\partial W}{\partial u_r} - \left(\frac{\partial W}{\partial u_{r,i}} \right)_{,i} + \left(\frac{\partial W}{\partial u_{r,ij}} \right)_{,ij} - \lambda \frac{\partial g}{\partial u_r} + \left(\lambda \frac{\partial g}{\partial u_{r,i}} \right)_{,i} = 0. \quad (\text{A.0.6})$$

where λ is a Lagrange-multiplier field.

The heterogeneity of the system is represented by the explicit dependence of W on \mathbf{x} . Configurational forces are energetic forces conjugate to rearrangements of the heterogeneity of the system. A rearrangement is described by a group of mappings $\varphi_\epsilon : \mathbb{R}^n \rightarrow \mathbb{R}^n$, $\epsilon \geq 0$, such that $\varphi_\epsilon \rightarrow \text{id}$ as $\epsilon \rightarrow 0$. A rearrangement defines the family of energy functionals:

$$E_\epsilon(\mathbf{u}) = \int W(\varphi_\epsilon(\mathbf{x}), \mathbf{u}(\mathbf{x}), D\mathbf{u}(\mathbf{x}), D^2\mathbf{u}(\mathbf{x})) dx. \quad (\text{A.0.7})$$

The configurational force corresponding to the rearrangement is

$$F(\mathbf{v}) = \left[\frac{d}{d\epsilon} E_\epsilon(\mathbf{u}_\epsilon) \right]_{\epsilon=0}, \quad (\text{A.0.8})$$

where \mathbf{u}_ϵ denotes a sequence of minimizers of the functionals $E_\epsilon(\mathbf{u})$, and

$$\mathbf{v}(\mathbf{x}) = \left[\frac{d}{d\epsilon} \varphi_\epsilon(\mathbf{x}) \right]_{\epsilon=0} \quad (\text{A.0.9})$$

is the infinitesimal generator of the rearrangement group. A formal evaluation of (A.0.8) gives

$$F(\mathbf{v}) = \int \left[\left(\frac{\partial W}{\partial x_i} \right)_{\text{exp}} v_i + \frac{\partial W}{\partial u_r} w_r + \frac{\partial W}{\partial u_{r,i}} w_{r,i} + \frac{\partial W}{\partial u_{r,ij}} w_{r,ij} \right] dx, \quad (\text{A.0.10})$$

where the label *exp* signifies that the partial derivatives are taken with respect to the *explicit* dependence of W on \mathbf{x} , and

$$\mathbf{w} = \left[\frac{d}{d\epsilon} \mathbf{u}_\epsilon(\mathbf{x}) \right]_{\epsilon=0}. \quad (\text{A.0.11})$$

Since, by assumption, all minimizers \mathbf{u}_ϵ satisfy the internal constraint $g(\mathbf{x}, \mathbf{u}(\mathbf{x}), D\mathbf{u}(\mathbf{x})) = 0$ in (A.0.2), it follows that \mathbf{w} is admissible in the sense of (A.0.5), and thus stationarity gives

$$F(\mathbf{v}) = \int \left(\frac{\partial W}{\partial x_i} \right)_{\text{exp}} v_i dx. \quad (\text{A.0.12})$$

The chain of identities

$$\left(\frac{\partial W}{\partial x_i} \right)_{\text{exp}} = \frac{\partial W}{\partial x_i} - \frac{\partial W}{\partial u_r} u_{r,i} - \frac{\partial W}{\partial u_{r,j}} u_{r,ji} - \frac{\partial W}{\partial u_{r,jk}} u_{r,jki} = \quad (\text{A.0.13a})$$

$$\frac{\partial W}{\partial x_i} - \frac{\partial W}{\partial u_r} u_{r,i} - \left(\frac{\partial W}{\partial u_{r,j}} u_{r,i} \right)_{,j} + \left(\frac{\partial W}{\partial u_{r,j}} \right)_{,j} u_{r,i} - \frac{\partial W}{\partial u_{r,jk}} u_{r,jki} = \quad (\text{A.0.13b})$$

$$\frac{\partial W}{\partial x_i} + \left\{ \left(\frac{\partial W}{\partial u_{r,jk}} \right)_{,jk} - \lambda \frac{\partial g}{\partial u_r} + \left(\lambda \frac{\partial g}{\partial u_{r,j}} \right)_{,j} \right\} u_{r,i} - \left(\frac{\partial W}{\partial u_{r,j}} u_{r,i} \right)_{,j} - \frac{\partial W}{\partial u_{r,jk}} u_{r,jki} = \quad (\text{A.0.13c})$$

$$\frac{\partial W}{\partial x_i} - \left[\left(\frac{\partial W}{\partial u_{r,j}} - \lambda \frac{\partial g}{\partial u_{r,j}} \right) u_{r,i} \right]_{,j} + \left(\frac{\partial W}{\partial u_{r,jk}} \right)_{,jk} u_{r,i} - \frac{\partial W}{\partial u_{r,jk}} u_{r,jki} = \quad (\text{A.0.13d})$$

$$\left\{ W \delta_{ij} - \left[\frac{\partial W}{\partial u_{r,j}} - \lambda \frac{\partial g}{\partial u_{r,j}} - \left(\frac{\partial W}{\partial u_{r,jk}} \right)_{,k} \right] u_{r,i} - \frac{\partial W}{\partial u_{r,jk}} u_{r,ki} \right\}_{,j} \equiv P_{ij,j} \quad (\text{A.0.13e})$$

shows that the configuration force (A.0.12) may be expressed in the conservation form

$$F(\mathbf{v}) = \int P_{ij,j} v_i dx, \quad (\text{A.0.14})$$

in terms of the energy-momentum tensor

$$P_{ij} = W \delta_{ij} - \left[\frac{\partial W}{\partial u_{r,j}} - \lambda \frac{\partial g}{\partial u_{r,j}} - \left(\frac{\partial W}{\partial u_{r,jk}} \right)_{,k} \right] u_{r,i} - \frac{\partial W}{\partial u_{r,jk}} u_{r,ki}. \quad (\text{A.0.15})$$

We note that (A.0.13a) follows from a direct application of the chain rule of differentiation, (A.0.13b) follows from the properties of partial differentiation, (A.0.13c) is obtained using the Euler-Lagrange equations (A.0.6), (A.0.13d) is obtained using the admissibility condition (A.0.5) replacing w_r by $u_{r,i}$ for fixed i , and (A.0.13e) follows again from the properties

of partial differentiation.

Appendix B

An iterative front-relaxation algorithm

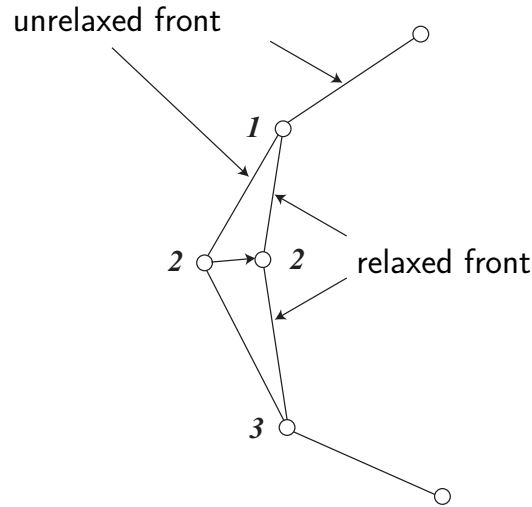


Figure B.1: Local stencil for the relaxation iteration.

In this appendix we describe a local iterative scheme which relaxes an unstable arc of front, i.e., an arc where $\kappa > r^{-1}$, to an equilibrium interface. The objective is to introduce an iteration whose fixed point satisfies equations (3.3.10). The local stencil used in the iteration is shown in Figure B.1. The iteration moves one node of the unrelaxed front in turn to a new position in such a way that the arc defined by three consecutive points on the new front, e.g., points 1, 2, and 3 in Figure B.1, approximates, to within the accuracy of the discretization, a solution of (3.3.10). We begin by re-writing these equations in the form

$$\frac{\partial r}{\partial \sin \varphi} = r, \quad -\frac{\partial z}{\partial \cos \varphi} = r, \quad (\text{B.0.1})$$

and proceed to discretize them by the midpoint rule, with the result

$$\frac{r_3 - r_1}{\sin \varphi_3 - \sin \varphi_1} = \frac{r_1 + r_3}{2}, \quad \frac{z_3 - z_1}{\cos \varphi_3 - \cos \varphi_1} = -\frac{r_1 + r_3}{2}. \quad (\text{B.0.2})$$

These equations may be solved for the unknowns φ_1 and φ_3 , i.e., for the polar angles of the tangent to the equilibrium interface at points 1 and 3. Next we set

$$\varphi_2 = \frac{\varphi_1 + \varphi_3}{2}, \quad (\text{B.0.3})$$

and proceed to compute the coordinates of the relaxed node as

$$r_2 = \frac{1}{2} [r_1 + r_1(\sin \varphi_2 - \sin \varphi_1) + r_3 + r_3(\sin \varphi_2 - \sin \varphi_3)], \quad (\text{B.0.4a})$$

$$z_2 = \frac{1}{2} [z_1 - r_1(\cos \varphi_2 - \cos \varphi_1) + z_3 - r_3(\cos \varphi_2 - \cos \varphi_3)]. \quad (\text{B.0.4b})$$

In calculations, we relax each node of the front in turn, which completes one iteration, and we iterate until convergence is achieved to within a pre-specified tolerance.

Bibliography

S.S. Antman.

Nonlinear Problems of Elasticity.

Springer-Verlag, 1995.

P.G. Arscott, A.-L. Li, and V.A. Bloomfield.

Condensation of DNA by trivalent cations. 1. Effects of DNA length and topology on the size and shape of condensed particles.

Biopolymers, 30:619–630, 1990.

L.W. Black, W.W. Newcomb, J.W. Boring, and J.C. Brown.

Ion etching of bacteriophage-T4—support for a spiral-fold model of packaged DNA.

Proceedings of the National Academy of Sciences of the United States of America, 82 (23):7960–7964, 1985.

V.A. Bloomfield.

DNA condensation.

Current Opinion in Structural Biology, 6(3):334–341, 1996.

V.A. Bloomfield.

DNA condensation by multivalent cations.

Biopolymers, 44(3):269–282, 1997.

D.H. Boal.

Mechanics of the Cell.

Cambridge University Press, 2002.

C. Bouchiat and M. Mezard.

- Elastic rod model of a supercoiled DNA molecule.
The European Physical Journal E, 2:377–402, 2000.
- M.E. Cerritelli, N.Q. Cheng, A.H. Rosenberg, C.E. McPherson, F.P. Booy, and A.C. Steven.
 Encapsidated conformation of bacteriophage T7 DNA.
Cell, 91(2):271–280, 1997.
- B. Dacorogna.
Direct Methods in the Calculus of Variations.
 Springer-Verlag, 1989.
- G. Dal Maso.
An Introduction to Γ -convergence.
 Birkhäuser, Boston, 1993.
- A. de Simone, R.V. Kohn, S. Müller, and F. Otto.
 Magnetic microstructures—a paradigm of multiscale problems.
 In J.M. Ball and J.C.R. Hunt, editors, *ICIAM 99*, pages 175–190. Oxford University Press, 2000.
- W.C. Earnshaw and S.C. Harrison.
 DNA arrangement in isometric phage heads.
Nature, 268(5621):598–602, 1977.
- L.C. Evans.
Partial Differential Equations.
 American Mathematical Society, Providence, R.I., 1998.
- W.M. Gelbart, R.F. Bruinsma, P.A. Pincus, and V.A. Parsegian.
 DNA-inspired electrostatics.
Physics Today, 53(9):38–44, 2000.
- M.E. Gurtin.
Configurational Forces as Basic Concepts of Continuum Physics.
 Springer-Verlag, New York, 2000.

N.V. Hud.

Double-stranded DNA organization in bacteriophage heads—an alternative toroid-based model.

Biophysical Journal, 69(4):1355–1362, 1995.

N.V. Hud, K.H. Downing, and R. Balhorn.

A constant radius of curvature model for the organization of DNA in toroidal condensates.

Proceedings of the National Academy of Sciences of the United States of America, 92: 3581–3585, 1995.

J. Kindt, S. Tzlil, A. Ben-Shaul, and W.M. Gelbart.

DNA packaging and ejection forces in bacteriophage.

Proceedings of the National Academy of Sciences of the United States of America, 98 (24):13671–13674, 2001.

S. Kirkpatrick, C.D. Gelatt, and Vecchi M.P.

Optimization by simulated annealing.

Science, 220(4598):671–680, 1983.

D.G. Luenberger.

Linear and Nonlinear Programming.

Addison-Wesley, 1989.

N. Metropolis, A.W. Rosenbluth, M.N. Rosenbluth, A.H. Teller, and E. Teller.

Equation of state calculations by fast computing machines.

Journal of Chemical Physics, 21(6):1087–1092, 1953.

J.D. Moroz and P. Nelson.

Entropic elasticity of twist-storing polymers.

Macromolecules, 31:6333–6347, 1998.

J. Nocedal and S.J. Wright.

Numerical Optimization.

Springer-Verlag, 1999.

T. Odijk.

Hexagonally packed DNA within bacteriophage T7 stabilized by curvature stress.

Biophysical Journal, 75:1223–1227, 1998.

N.H. Olson, M. Gingery, F.A. Eiserling, and T.S. Baker.

The structure of isometric capsids of bacteriophage T4.

Virology, 279(2):385–391, 2001.

V.A. Parsegian, R.P. Rand, N.L. Fuller, and D.C. Rau.

Osmotic stress for the direct measurement of intermolecular forces.

Methods in Enzymology, 127:400–416, 1986.

P.K. Purohit, J. Kondev, and R. Phillips.

Mechanics of DNA packaging in viruses.

Proceedings of the National Academy of Sciences of the United States of America, 100
(6):3173–3178, 2003.

D.C. Rau, B. Lee, and V.A. Parsegian.

Measurement of the repulsive force between polyelectrolyte molecules in ionic solution:
Hydration forces between parallel DNA double helices.

Proceedings of the National Academy of Sciences of the United States of America, 81:
2621–2625, 1984.

D.C. Rau and V.A. Parsegian.

Direct measurement of temperature-dependent solvation forces between DNA double
helices.

Biophysical Journal, 61(1):260–271, 1992.

K.E. Richards, R.C. Williams, and R. Calendar.

Mode of DNA packing within bacteriophage heads.

J. Mol. Biol., 78:255–259, 1973.

S.C. Riemer and V.A. Bloomfield.

Packaging of DNA in bacteriophage heads—some considerations on energetics.
Biopolymers, 17(3):785–794, 1978.

R.T. Rockafellar.

Convex Analysis.
Princeton University Press, Princeton, N.J., 1970.

P. Salamon, P. Sibani, and R. Frost.

Facts, Conjectures, and Improvements for Simulated Annealing.
Society for Industrial and Applied Mathematics, 2002.

A.A. Simpson, Y.Z. Tao, P.G. Leiman, M.O. Badasso, Y.N. He, P.J. Jardine, N.H. Olson,
M.C. Morais, S. Grimes, D.L. Anderson, T.S. Baker, and M.G. Rossmann.
Structure of the bacteriophage $\phi 29$ DNA packaging motor.
Nature, 408(6813):745–750, 2000.

D.E. Smith, S.J. Tans, S.B. Smith, S. Grimes, D.L. Anderson, and C. Bustamante.
The bacteriophage $\phi 29$ portal motor can package DNA against a large internal force.
Nature, 413(6857):748–752, 2001.

S.B. Smith, L. Finzi, and C. Bustamante.

Direct mechanical measurements of the elasticity of single DNA-molecules by using
magnetic beads.
Science, 258(5085):1122–1126, 1992.

T.R. Strick, J.-F. Allemand, A. Bensimon, and V. Croquette.

The elasticity of a single supercoiled DNA molecule.
Science, 271:1835–1837, 1996.

H. Szu and R. Hartley.

Fast simulated annealing.
Physics Letters A, 122(3,4):157–162, 1987.

S. Tzlil, J. Kindt, W.M. Gelbart, and A. Ben-Shaul.

Forces and pressures in DNA packaging and release from viral capsids.

Biophysical Journal, 84:1616–1627, 2003.

J. Ubbink and T. Odijk.

Deformation of toroidal DNA condensates under surface stress.

Europhysics Letters, 33(5):353–358, 1996.